

AD-A094 068

ILLINOIS UNIV AT URBANA-CHAMPAIGN ELECTROMAGNETICS LAB  
A STUDY OF MICROSTRIP ANTENNA ELEMENTS AND ARRAYS (U)

F/6 9/5

DEC 80 Y T LO, W F RICHARDS, P SIMON

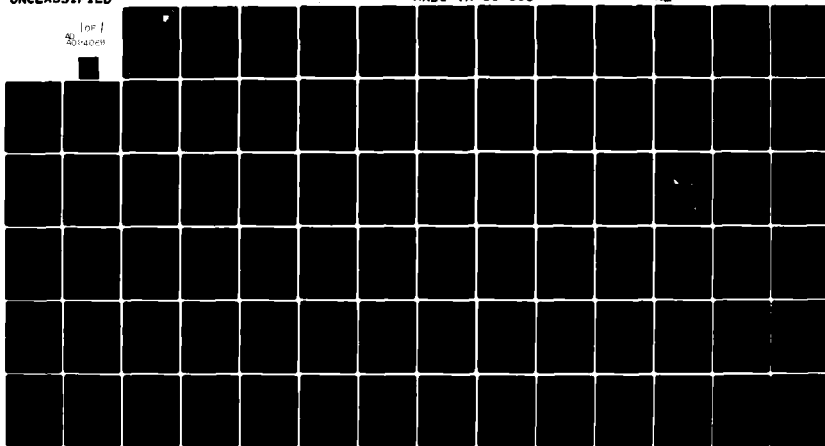
F19628-78-C-0025

UNCLASSIFIED

RADC-TR-80-363

NL

Top 1  
80-4028



END  
DATE FILMED  
JFHC

AD A094068

RADC-TR-80-363  
Interim Report  
December 1980

LEVEL II



12

10-5

## A STUDY OF MICROSTRIP ANTENNA ELEMENTS AND ARRAYS

University of Illinois at Urbana-Champaign

Y.T. Lo  
W.F. Richards  
P. Simon

DTIC  
ELECTED  
S JAN 23 1981  
E

APPROVED FOR PUBLIC RELEASE; DISTRIBUTION UNLIMITED

ROME AIR DEVELOPMENT CENTER  
Air Force Systems Command  
Griffiss Air Force Base, New York 13441

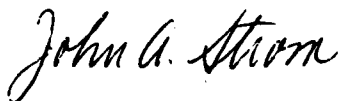
DDC FILE COPY

81 1 23 005

This report has been reviewed by the RADC Public Affairs Office (PA) and is releasable to the National Technical Information Service (NTIS). At NTIS it will be releasable to the general public, including foreign nations.

RADC-TR-80-363 has been reviewed and is approved for publication.

APPROVED:



JOHN A. STROM  
Project Engineer

APPROVED:



ALLAN C. SCHELL, Chief  
Electromagnetic Sciences Division

FOR THE COMMANDER:



JOHN P. HUSS  
Acting Chief, Plans Office

If your address has changed or if you wish to be removed from the RADC mailing list, or if the addressee is no longer employed by your organization, please notify RADC (EEAA) Hanscom AFB MA 01731. This will assist us in maintaining a current mailing list.

Do not return this copy. Retain or destroy.

UNCLASSIFIED

SECURITY CLASSIFICATION OF THIS PAGE (When Data Entered)

REPORT DOCUMENTATION PAGE		READ INSTRUCTIONS BEFORE COMPLETING FORM
1. REPORT NUMBER RADCTR-80-363	2. GOVT ACCESSION NO. AD-A094 068	3. RECIPIENT'S CATALOG NUMBER
4. TITLE (and Subtitle) A STUDY OF MICROSTRIP ANTENNA ELEMENTS AND ARRAYS		5. TYPE OF REPORT & PERIOD COVERED Interim Report
6. AUTHOR(s) Y. T. Lo W. F. Richards P. Simon		6. PERFORMING ORG. REPORT NUMBER N/A
7. PERFORMING ORGANIZATION NAME AND ADDRESS University of Illinois at Urbana-Champaign Department of Electrical Engineering/Electromagnetics Laboratory, Urbana IL 61801		8. CONTRACT OR GRANT NUMBER(s) F19628-78-C-0025
9. CONTROLLING OFFICE NAME AND ADDRESS Deputy for Electronic Technology (RADC/EEAA) Hanscom AFB MA 01731		10. PROGRAM ELEMENT, PROJECT, TASK AREA & WORK UNIT NUMBERS 61102F 2305J323
11. MONITORING AGENCY NAME & ADDRESS (if different from Controlling Office) Same		12. REPORT DATE December 1980
		13. NUMBER OF PAGES 82
14. DISTRIBUTION STATEMENT (of this Report) Approved for public release; distribution unlimited.		15. SECURITY CLASS. (of this report) UNCLASSIFIED
		16. DECLASSIFICATION/DOWNGRADING SCHEDULE N/A
17. DISTRIBUTION STATEMENT (of the abstract entered in Block 20, if different from Report) Same		
18. SUPPLEMENTARY NOTES RADC Project Engineer: John A. Strom (EEAA)		
19. KEY WORDS (Continue on reverse side if necessary and identify by block number) Microstrip antennas microstrip antenna arrays		
20. ABSTRACT (Continue on reverse side if necessary and identify by block number) Thin microstrip antennas have many unique and attractive properties, but their operation is much limited in bandwidth. So far the only effective known method for broadening the bandwidth is to either use a thick substrate, or equivalently operate the antenna at high frequencies. In this report an attempt is made to develop a procedure for array design, in particular, to determine whether or not the band of operation could be broadened by using a small array of two elements of slightly different dimensions. (Cont'd)		

DD FORM 1 JAN 73 1473

UNCLASSIFIED

SECURITY CLASSIFICATION OF THIS PAGE (When Data Entered)

UNCLASSIFIED

SECURITY CLASSIFICATION OF THIS PAGE(When Data Entered)

Item 20 (Cont'd)

By broadband, it is meant that the antenna must have over the bandwidth, first, an input impedance variation within a certain prescribed SWR (say 3:1); second a stable pattern (in particular a stable beam-pointing direction); third a small variation in gain (or efficiency); and, in some applications, small variations in beamwidth and sidelobe level. In this work only the first two fundamental performances are considered.

Insofar as the impedance is considered, the array design is essentially a circuit problem. Our theory based on the cavity model has previously shown that the element impedance can adequately be described by a Foster network representation, namely, a series circuit of infinitely many parallel resonant circuits, each corresponding to a mode of the cavity. For frequencies in the vicinity of a certain mode, the circuit can further be reduced to a single parallel resonant circuit of that mode in series with an inductance. Our earlier investigation has also shown that, except for very close spacings, the mutual coupling effect between elements can be ignored. Thus, for desired array impedance characteristics, it is a matter of realizing a certain element impedance transformation with proper strip line design. However, this does not guarantee a desired pattern characteristic. For the latter, one must evaluate the fields due to all the elements in the array with their relative excitation current magnitudes and phases determined from the circuit analysis. An algorithm is developed to accomplish both of these tasks, which is then used to search for the best design with a computer. The program is applied in particular to a design reported by Pues et al. [11]. Their claim of a stable pattern over about a 10% bandwidth has not been substantiated by this means.

In the course of this investigation, the question of characterization of small discontinuity in the microstrip line to coaxial cable transition arises. Some useful and interesting findings are included in this report. In addition, for completeness, a detailed account for the development of the antenna element theory is also reviewed, which hopefully would clear up many misunderstandings expressed by some readers of our previous work.

UNCLASSIFIED

SECURITY CLASSIFICATION OF THIS PAGE(When Data Entered)

## TABLE OF CONTENTS

<u>CHAPTER</u>	<u>PAGE</u>
I. INTRODUCTION .....	1
II. THE RECTANGULAR MICROSTRIP ANTENNA .....	4
III. CIRCULAR POLARIZATION IN MICROSTRIP ANTENNAS .....	26
IV. CHARACTERIZATION OF THE MICROSTRIP LINE AND COAXIAL TRANSITION .....	41
V. TWO ELEMENT ARRAY .....	58
VI. SUMMARY .....	72
REFERENCES .....	73

Accession For	
NTIS GRA&I	<input checked="" type="checkbox"/>
DATA TAB	<input type="checkbox"/>
UNCLASSIFIED	<input type="checkbox"/>
Classification	
Date Entered	
Date Received	
Serial No. Codes	
Date	
Date	
A	

## LIST OF FIGURES

<u>FIGURE NO.</u>		<u>PAGE</u>
2.1	The microstrip antenna .....	5
2.2	Illustration of localization of $K_s$ to patch boundary ..	12
2.3	Impedance of a rectangular microstrip antenna .....	22
2.4	Circuit representations for microstrip antennas .....	24
3.1	Microstrip antennas capable of producing circular polarization .....	28
3.2	Relative pole positions in the complex K plane .....	30
3.3	Elevation patterns taken with rotating dipoles for nearly square microstrip antenna .....	31
3.4	Double tuned antenna .....	34
3.5	Impedance of double tuned antenna .....	35
3.6	CP patterns for double tuned antenna .....	36
3.7	Degradation of axial ratio with normalized frequency ..	38
3.8	Measured response of rotating dipole and plot of axial ratio for nearly square antenna .....	39
4.1	The microstrip transmission line .....	42
4.2	Measured return loss and phase of $\Gamma$ , the voltage reflection coefficient, versus distance from open circuited end of a microstrip fifty ohm line at 800 MHz .....	46
4.3	SMA semi-rigid coaxial transition .....	49
4.4	Type N coaxial transition .....	50
4.5	Equivalent circuit for determining scattering parameters of coaxial transition .....	52

<u>FIGURE NO.</u>		<u>PAGE</u>
4.6	Data used to determine $S_{11}$ at 800 MHz plotted on central portion of the Smith chart .....	54
4.7	Data of Fig. 4.2 with the effect of the scattering parameters removed .....	56
5.1	Definitions for two element array .....	59
5.2	Measured and computed Z for element #1 with $d^{(1)} = 49.5$ cm .....	63
5.3	Measured and computed Z for two element array ... ....	64
5.4	Measured and computed radiation pattern for array at 765 MHz .....	65
5.5	Measured and computed radiation pattern for array at 800 MHz .....	66
5.6	Measured and computed radiation pattern for array at 810 MHz .....	67
5.7	Measured and computed radiation pattern for array at 820 MHz .....	68
5.8	Pattern obtained from design algorithm of Ref. [11] at 9.45 GHz .....	70

#### LIST OF TABLES

4.1	Measured scattering parameter; .....	55
5.1	Array cimensions .....	61

## I. INTRODUCTION

The desirable qualities of microstrip antennas, such as light weight, low profile, ease of manufacture, conformability, and low cost, make them attractive choices for many applications. In fact, the microstrip is the only type of antenna which can claim all of these attributes in a single package. It comes as no surprise then that much recent activity has centered on analyzing the microstrip antenna.

The early designs utilizing microstrip elements were based on empirical knowledge of the antenna's properties [1]. The antenna input impedance was first measured, then a matching network was designed to match the antenna to fifty ohms. The antenna was then rebuilt to incorporate the matching network on the same substrate. Clearly, this is an inefficient procedure, and it was not long before a theory was developed to predict impedance and pattern information.

The first analysis of the microstrip radiator [2,3] modeled it as two radiating slots connected by a low impedance transmission line. This theory is limited in that it can only be applied to rectangular patches, and fails to predict the impedance locus accurately, in particular, its shift into the inductive side of the Smith Chart. Moreover, this theory cannot predict the occurrence of radiation from all four sides of a singly fed patch, an important mechanism for many commonly excited modes.

Recently, a more comprehensive theory has been presented by Lo and Richards [4-6] which enables one to predict the important properties of a wide variety of microstrip antennas in detail. This theory treats the antenna as a resonant cavity, bounded above and below by an electric conductor, and on the perimeter by a magnetic conductor. By means of this theory, the impedance locus and radiation

patterns for any feed location may be accurately predicted. The theory has also been extended to multiport analysis and, in this report, is extended to the design of circularly polarized microstrip antennas.

Circular Polarization (CP) has been reported in a variety of microstrip antennas [5,7-9]. Experimental work was recently reported on a class of CP antennas derived from disk and square antennas by cutting slots in their interiors or corners off their perimeters. For all these antennas, the theory presented in this paper provides an explanation for the mechanism of antenna operation, and in some cases, provides a means for predicting the exact dimensions needed for achieving CP operation. This is important because CP operation is possible only for a very narrow band of frequency, and without a theoretical prediction, many painstaking cut-and-trials would be necessary. In this report a new type of CP antenna is described. The operating frequency of this antenna may be tuned over a relatively wide bandwidth. Also, the antenna polarization is electronically adjustable from CP to linear polarization to CP of the opposite sense, or any arbitrary polarization within these limits.

A major limitation of the microstrip antenna is narrow bandwidth, a characteristic of all resonant structures. Several methods of bandbroadening have been considered in the literature, such as stacking [10] or array structures [11]. Stacked structures suffer the disadvantage of greater overall antenna height and increased cost due to manufacturing complications. Furthermore, it seems likely that increases in bandwidth gained by stacking antennas could be realized more conveniently by simply increasing the substrate thickness of a conventional microstrip antenna by an equivalent amount. Since current interest is focused on very thin structures, the stacking method is not examined in this report. Instead, a corporately fed array of two microstrip elements of slightly different dimensions is considered. This approach is inspired by the use of a

multiple tuning circuit for a broadband operation and has been experimentally explored by Van de Capelle [11]. The objective of this study is to systematically develop a design algorithm such that the best design can be obtained without the painstaking trial-and-error method to actually test many antennas for a correct array configuration.

A computer analysis is conducted, modeling the array elements as equivalent networks and using the transmission line theory to calculate the input impedance of the array feed. After computing the currents at each element, the radiation pattern is also computed. The design goals are a stable pattern, good efficiency, and low VSWR over a wider bandwidth than possible with a single element.

## II. THE RECTANGULAR MICROSTRIP ANTENNA

Referring to Fig. 2.1, it is seen that a microstrip antenna consists of a metallic patch and groundplane, separated a small distance  $t$  by a dielectric sheet. The metal is characterized by conductivity  $\sigma$ , and the dielectric by permeability  $\mu_0$ , permittivity  $\epsilon = \epsilon_0 \epsilon_r$ , and loss tangent  $\delta$ . A rigorous numerical solution for the fields in this structure due to a given excitation current  $\vec{J}$  is possible using a procedure such as the method of moments. However, a much simpler formulation is found to yield results of sufficient accuracy for nearly all applications, while providing a great deal of physical insight into the operation of the antenna. This theory is based on the resonant cavity model of the microstrip antenna, developed at the University of Illinois [4-6]. Although the theory was reported in the course of its development, the lack of details and unification in these presentations has caused some misunderstanding among the workers in the area. In the following, for completeness, this theory is reviewed with emphasis on the detailed argument which has led to the model and on the detailed analysis which will be used for the computation later in this thesis.

Taking the  $z$ -axis as the normal to the plane containing the patch, note the close proximity between the patch element and ground plane (typically a few thousandths of a wavelength in free space). This suggests that there is no variation of the fields with  $z$  in the region between the patch and groundplane (hereafter referred to as the "interior region"). Since the tangential electric field must vanish on the (nearly) perfectly conducting metal surfaces, one may thus conclude that  $\hat{E} = \hat{z}E_z$  in this region. From Maxwell's Equation, one finds that  $\hat{H}$ , which is proportional to  $\text{curl } \hat{E}$  in the source-free interior region, is entirely transverse to  $\hat{z}$ .

Now consider the electric surface current,  $\vec{J}_s$ , flowing on the underside of the patch. At the perimeter of the patch,  $\vec{J}_s$  must have no component in the direction

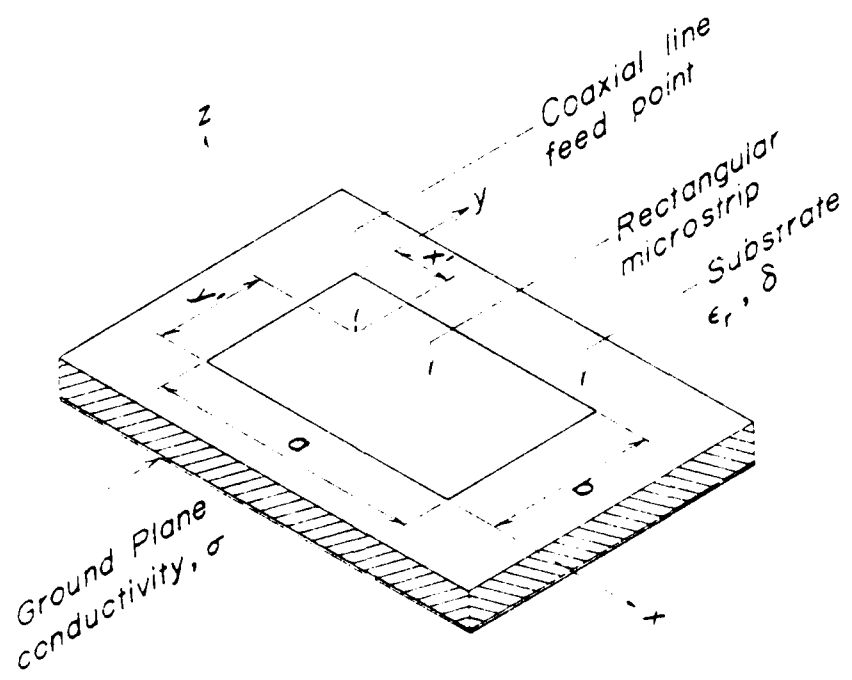
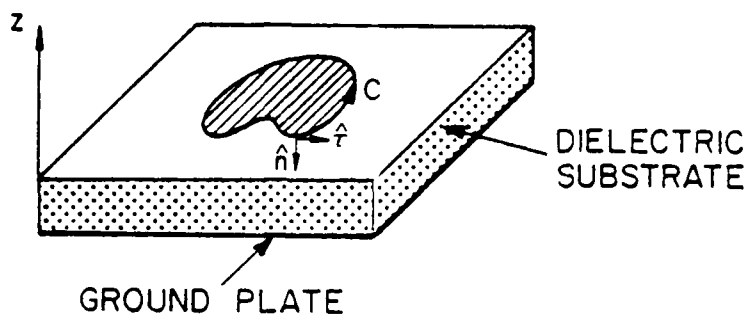


Figure 2.1. The microstrip antenna. (a) Generalized microstrip antenna; (b) Coordinate system for rectangular microstrip antenna.

of the normal to the boundary,  $\hat{n}$ . Assuming the patch to be perfectly conducting, the surface current and the magnetic field are related by the boundary condition:

$$\vec{J}_s = -\hat{z} \times \vec{H}|_{z=0} . \quad (2.1)$$

Crossing  $\hat{z}$  into both sides of Eq. (2.1) gives

$$\hat{z} \times \vec{J}_s = \hat{z} \times (-\hat{z} \times \vec{H}) = -\hat{z}(\hat{z} \cdot \vec{H}) + \vec{H}(\hat{z} \cdot \hat{z}) = \vec{H} . \quad (2.2)$$

Let  $\hat{n}$ ,  $\hat{\tau}$ , and  $\hat{z}$  form a triad so that  $\hat{n} \times \hat{\tau} = \hat{z}$  as shown in Fig. 1.1a. Then  $\vec{J}_s$  may be decomposed into components tangential to and normal to the boundary, i.e.,  $\vec{J}_s = (\hat{\tau}\hat{\tau} + \hat{n}\hat{n}) \cdot \vec{J}_s$ . Let the boundary be denoted by C. Since  $\hat{n} \cdot \vec{J}_s|_C = 0$  for any point on C, Eq. (2.2) becomes

$$\hat{z} \times \hat{\tau} | J_s |_C = -\hat{n} | J_s |_C = \vec{H}|_C . \quad (2.3)$$

Eq. (2.3) states that  $\vec{H}$  has only a normal component at the boundary, or that  $H_{tan} = 0$ . This implies that the boundary condition is effectively a perfect magnetic conducting (PMC) wall along C.

In accordance with the preceding discussion, the region between the patch and ground plane may be treated as a cavity bounded above and below by perfect electric conducting (PEC) walls and around its perimeter by PMC material. Obviously, such a closed structure would not radiate and would present a purely reactive input impedance if the substrate is lossless. However, following a commonly used approximation in antenna analysis, one may assume that the fields in the cavity are not greatly different from those in the interior region of the actual microstrip antenna. From a knowledge of these fields, one may compute the radiation pattern, total radiated power, and impedance characteristics of the antenna.

Methods of analyzing two dimensional cavities are widely known [12,13]. In this report the Green's function  $G(x,y;x',y')$ , i.e., the electric field at  $(x,y)$  due to  $\vec{J} = \hat{z}\delta(x - x')\delta(y - y')$ , the unit spatial impulse source at  $(x',y')$  in the cavity, will be found first. Then, by applying superposition, the fields due to an arbitrary  $\vec{J} = \hat{z}f(x,y)$  may be found.

The preceding discussion has been general in that it assumes nothing about the shape of the patch. The discussion will now be limited to the rectangular geometry shown in Fig. 2.1b. Adopting the coordinate system shown in that figure, Maxwell's equations for the interior region become

$$\nabla \times \vec{E} = -j\omega\mu\vec{H} \quad (2.4)$$

$$\nabla \times \vec{H} = j\omega\epsilon(1 - j\delta) \vec{E} + \hat{z}\delta(x - x')\delta(y - y') \quad (2.5)$$

where  $\epsilon$  and  $\delta$  are respectively the permittivity and loss tangent of the substrate.

The boundary conditions on  $\vec{H}$  are

$$H_x(x,0) = H_x(x,b) = H_y(0,y) = H_y(a,y) = 0 \quad . \quad (2.6)$$

Let  $\vec{E} = \hat{z}G$ . Then, substituting this expression into Eq. (2.4), remembering that  $\vec{E}$  is independent of  $z$ , gives

$$\nabla G \times \hat{z} = \hat{x} \frac{\partial G}{\partial y} - \hat{y} \frac{\partial G}{\partial x} = -j\omega\mu\vec{H} \quad . \quad (2.7)$$

The boundary conditions (2.6) may now be written for  $G$ :

$$\left. \frac{\partial G}{\partial y} \right|_{y=0} = \left. \frac{\partial G}{\partial y} \right|_{y=b} = \left. \frac{\partial G}{\partial x} \right|_{x=0} = \left. \frac{\partial G}{\partial x} \right|_{x=a} = 0 \quad . \quad (2.8)$$

The wave equation which  $\vec{E}$  must satisfy is easily found from (2.4) and (2.5) to be:

$$\nabla^2 \vec{E} + k^2 \vec{E} = j\omega\mu\vec{J} + \frac{j}{\omega\epsilon(1 - j\delta)} \nabla \nabla \circ \vec{J} \quad (2.9)$$

where  $k^2 = \omega_0^2 \mu_0 (1 - j\delta)$ . Substituting expressions for  $\vec{E}$  and  $\vec{J}$  into Eq. (2.9) gives

$$\nabla^2 G + k^2 G = j\omega_0 \delta(x - x') \delta(y - y') . \quad (2.10)$$

Eqs. (2.10) and (2.8) comprise the two-dimensional boundary value problem.

The solution to the inhomogeneous problem (2.10) may be expressed in terms of the eigenfunctions and eigenvalues of the associated source-free problem. Using the separation of variables, it is found that the homogeneous equation obeying the given boundary conditions has solutions of the form

$$\psi_{mn} = A_{mn} \cos \frac{m\pi x}{a} \cos \frac{n\pi y}{b} . \quad (2.11)$$

The eigenfunction  $\psi_{mn}$  is a solution only when  $k^2$  takes the value of the corresponding eigenvalue  $k_{mn}^2$ , given by

$$k_{mn}^2 = \left( \frac{m\pi}{a} \right)^2 + \left( \frac{n\pi}{b} \right)^2 \quad m, n = 0, 1, 2, \dots . \quad (2.12)$$

The coefficients  $A_{mn}$  are arbitrary and for convenience are chosen so that the  $\psi_{mn}$  form an orthonormal set in the sense that

$$\int_{x=0}^{y=a} \int_{y=0}^{y=b} \psi_{mn} \psi_{pq} dy dx = \begin{cases} 1, & m=p \text{ and } n=q \\ 0, & \text{otherwise} \end{cases} . \quad (2.13)$$

Carrying out the normalization, one finds that

$$A_{mn} = \left( \frac{\varepsilon_{om} \varepsilon_{on}}{ab} \right)^{1/2} ; \quad \varepsilon_{op} = \begin{cases} 1, & p=0 \\ 2, & p \neq 0 \end{cases} . \quad (2.14)$$

To construct the solution to Eq. (2.10), the forcing function is first expanded in terms of the set of eigenfunctions (or modes)  $\{\psi_{mn}\}$ .

$$\nabla^2 G + k^2 G = \sum_{m,n=0}^{\infty} B_{mn} \psi_{mn} . \quad (2.15)$$

Temporarily postponing the evaluation of the coefficients  $B_{mn}$ , the solution to Eq. (2.15) may be immediately written as

$$G = \sum_{m,n=0}^{\infty} \frac{B_{mn} \psi_{mn}}{k^2 - k_{mn}^2} . \quad (2.16)$$

This may be verified by direct substitution into Eq. (2.15). It should be noted that  $k^2$  is never equal to  $k_{mn}^2$  since  $k^2$ , as given above, has a nonzero imaginary part in the physical problem and  $k_{mn}^2$  is pure real.

The evaluation of coefficients  $B_{mn}$  is trivial. Using the orthonormality of  $\{\psi_{mn}\}$  in Eq. (2.13), one finds

$$B_{mn} = j\omega\mu \iint \psi_{mn}(x,y) \delta(x - x') \delta(y - y') dx dy = j\omega\mu \psi_{mn}(x',y') \quad (2.17)$$

Therefore,  $G$ , the solution to Eq. (2.10), is

$$G(x,y,x',y') = j\omega\mu \sum_{m,n=0}^{\infty} \frac{\psi_{mn}(x,y) \psi_{mn}(x',y')}{k^2 - k_{mn}^2} \quad (2.18)$$

To model the microstrip feed line or coaxial feed, the actual current source is taken to be a one amp ribbon of  $\hat{z}$ -directed electric current of width  $d$  and centered at the point  $(x',y')$ , i.e.,

$$\vec{J}(x,y) = \hat{z}\delta(y - y')[u(x - x' + \frac{d}{2}) - u(x - x' - \frac{d}{2})]/d \quad (2.19)$$

where  $u(x)$  is the unit step function equal to 0 for  $x < 0$ , and 1 for  $x > 0$ .

Using superposition,  $E_z$  due to this source is computed:

$$E_z(x,y) = \int_{y''=0}^b \int_{x''=0}^a G(x,y,z'',y'') J_z(x'',y'') dx'' dy'' \quad (2.20)$$

$$= \frac{j\omega\mu}{d} \sum_{m,n=0}^{\infty} \frac{\psi_{mn}(x,y)}{k^2 - k_{mn}^2} \frac{\epsilon_0 \epsilon_{\text{on}}}{ab} \cos \frac{n\pi y'}{b} \int_{x''=x'-\frac{d}{2}}^{x''=x'+\frac{d}{2}} \cos \frac{m\pi x''}{a} dx'' \quad (2.21)$$

$$= \frac{j\omega\mu}{d} \sum_{m,n=0}^{\infty} \frac{\epsilon_{om}\epsilon_{on}}{ab} \frac{\cos \frac{n\pi y'}{b} \psi_{mn}(x,y)}{k^2 - k_{mn}^2} \left\{ 2 \cos \frac{m\pi x'}{a} \sin \frac{m\pi d}{2a} \right\} \quad (2.22)$$

$$E_z(x,y) = j\omega\mu \sum_{m,n=0}^{\infty} \frac{\psi_{mn}(x,y) \psi_{mn}(x',y')}{k^2 - k_{mn}^2} j_0\left(\frac{m\pi d}{2a}\right) \quad (2.23)$$

where  $j_0(x) = \frac{\sin x}{x}$ .

Several comments are in order at this point. Examination of Eq. (2.23) indicates that if the frequency is such that the real part of  $k^2$  is equal to  $k_{mn}^2$ , then the MNth term in the series will become very large compared to any other single term in the series (except for degenerate modes), assuming  $\epsilon$  is sufficiently small. In the limiting case of zero losses, this term is unbounded. When the series becomes dominated by a single term in this manner, the system is said to be resonant and  $\psi_{mn}$  is referred to as the resonant mode. Also, note that the amplitude of each mode is partially determined by the feed location  $(x',y')$ . If the feed is located at a null of any mode, then that mode cannot be excited; it will have a coefficient of zero. Finally, the effect of feed width is manifest in the factor  $j_0\left(\frac{m\pi d}{2a}\right)$ , where  $j_0(x) = \frac{\sin x}{x}$ . It is seen that a source ribbon of narrow width  $d$  will excite larger amplitudes in high order modes than a ribbon of greater width.

In order to find the radiated power, one must relate the far field radiation to the modal fields just found in the cavity. An approximate method to accomplish this consists of the following steps:

1. Define an equivalent magnetic current line source  $\vec{K}_l = t\hat{n} \times \vec{E}|_c$ , where  $\hat{n}$  is the outward directed normal from  $c$ , the patch boundary, in the  $z=0$  plane.  $\vec{E}$  is computed from the cavity model.
2. Allow this magnetic current source to radiate in the presence of the PEC groundplane, at  $z = -t$ , ignoring the presence of the

dielectric. The far field electric vector potential,  $\vec{F}$ , is well known to be

$$\vec{F}(r, \theta, \phi) = \frac{-2e^{-jk_0 r}}{4\pi r} \iiint_{-\infty}^{\infty} \vec{K}(x, y, z) e^{jk_0(x \cos \phi \sin \theta + y \sin \phi \sin \theta + z \cos \theta)} dz dy dz \quad (2.24)$$

where  $k_0 = \frac{2\pi}{\lambda_0}$ ,  $\lambda_0$  = free space wavelength, and the factor "2" accounts for the image of  $\vec{K}$  due to the groundplane.

3. Compute  $\vec{E}(r, \theta, \phi) = jk_0(\hat{\theta}f_\phi - \hat{\phi}f_\theta)$ .

4. Compute radiated power  $P_r = 1/n \int_{\pi} r^2 |E|^2 d\Omega$ , where  $n = 377 \Omega$ .

The above approximate procedure is derived from Huygens' principle. One form of this famous theorem states that if all sources are placed inside a closed surface  $\Sigma$ , then the fields in the region exterior to  $\Sigma$  will be unchanged if their sources are taken to be  $\vec{K}_s = -\hat{n} \times \vec{E}|_{\Sigma}$ , with the interior of  $\Sigma$  filled with PEC material. For the present application, let the Huygens' surface be the  $z=0$  plane, so that  $\vec{K}_s = \hat{z} \times \vec{E}|_{z=0+}$ .  $\vec{K}_s$  will be zero over the area of the patch, since  $E_{tan}$  is zero there. Also,  $|\vec{K}_s|$  decreases extremely rapidly with distance from the edge of the patch, as shown in Fig. 2.2. Consider performing the integral of  $\vec{K}_s$  as indicated in Eq. (2.24) along the path AB in Fig. 2.2. The kernel of the transformation is nearly constant over this small linear path so that the result is essentially the line integral of  $\vec{K}_s$ . Since the distances involved are very small in terms of wavelengths and the magnetic field is negligibly small near the edge of the patch, a static approximation is thus employed:

$$\oint_{ABCDA} \vec{E} \cdot d\vec{l} \approx \int_A^B \vec{E} \cdot d\vec{l} + \int_B^C \vec{E} \cdot d\vec{l} \approx 0 \quad (2.25)$$

where points A, B, C, and D are defined in Fig. 2.2. Evaluating  $\vec{E} \cdot d\vec{l}$  for these paths gives

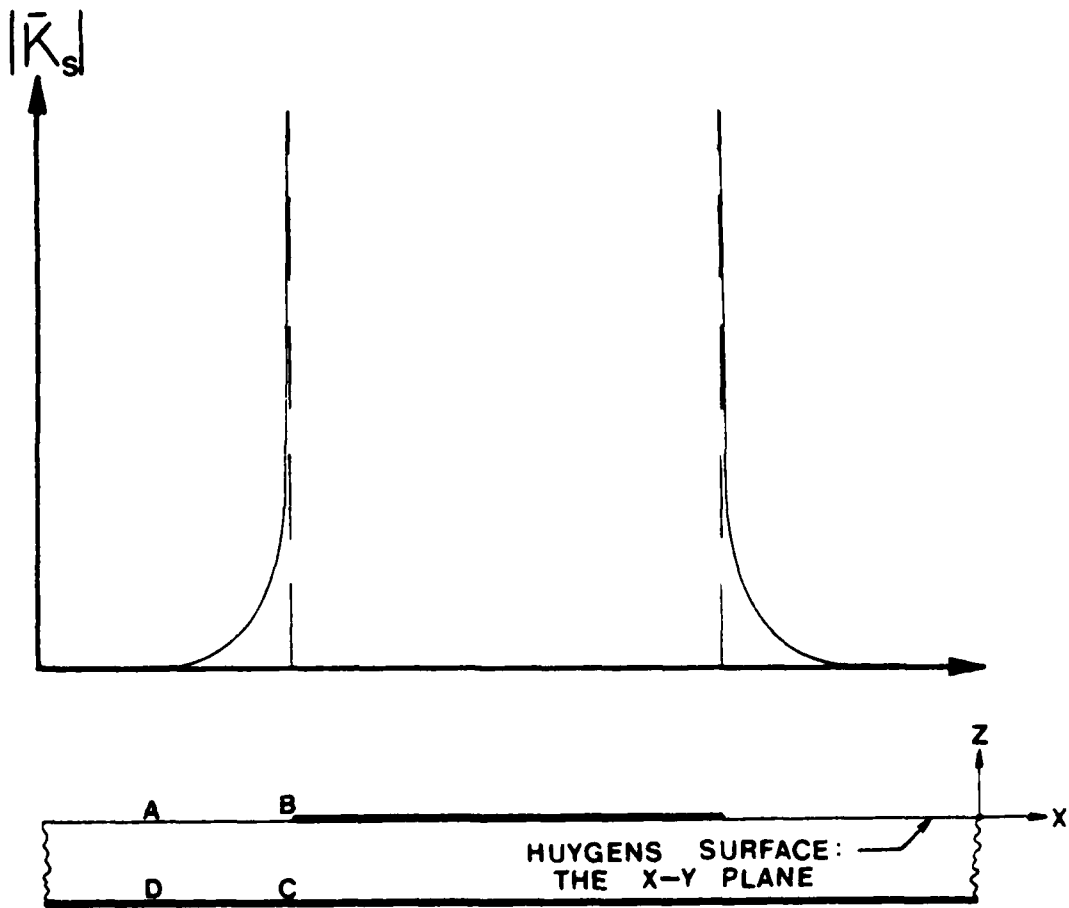


Figure 2.2. Illustration of localization of  $|K_s|$  to patch boundary.

$$\int_A^B E_x dx + \int_B^C E_z dz = C . \quad (2.26)$$

It is now assumed that  $\vec{E}$  lies in the plane of the figure, so that  $\vec{K}$  and  $\vec{E}$  are related by

$$\vec{K}_s = -\hat{z} \times \vec{E}|_{z=0} = -\hat{y} E_x . \quad (2.27)$$

Therefore, Eq. (2.26) may be rewritten in terms of  $\vec{K}$ :

$$\int_A^B \vec{K}_s dx + \hat{x} \times \int_B^C \hat{z} E_z dz = 0 . \quad (2.28)$$

Using  $E_z$  found for the cavity model and letting  $\hat{n}$  be the outward normal to  $C$ , the patch boundary, Eq. (2.28) becomes

$$\int_A^B \vec{K}_s dx = t \hat{n} \times \vec{E}|_C . \quad (2.29)$$

Thus, as an approximation to the unknown surface current  $\vec{K}_s$ , an equivalent line current  $\vec{K}_l = t \hat{n} \times \vec{E}|_C$  is defined as in step 1. Carrying out the procedure,  $\vec{K}_l$  is expressed in terms of  $E_z$ :

$$\begin{aligned} \vec{K}_l(x,y) = & t \{-\hat{y} \times \hat{z} E_z(x,0) \delta(y)[u(x) - u(x-a)] \\ & + \hat{y} \times \hat{z} E_z(x,b) \delta(y-b)[u(x) - u(x-a)] \\ & - \hat{x} \times \hat{z} E_z(0,y) \delta(x)[u(y) - u(y-b)] \\ & + \hat{x} \times \hat{z} E_z(a,y) \delta(x-a)[u(y) - u(y-b)]\} . \end{aligned} \quad (2.30)$$

After a small amount of manipulation:

$$\begin{aligned} \vec{K}_l = & t \{\hat{x}[E_z(x,b) \delta(y-b) - E_z(x,0) \delta(y)][u(x) - u(x-a)] \\ & + \hat{y}[E_z(0,y) \delta(x) - E_z(a,y) \delta(x-a)][u(y) - u(y-b)]\} \delta(z) . \end{aligned} \quad (2.31)$$

Consider for a moment  $\vec{K}_l$  due to a single mode  $E_z = \cos \frac{m\pi}{a} x \cos \frac{n\pi y}{b}$ :

$$\vec{K}_z = t \left\{ \hat{x} \left[ \cos \frac{m\pi x}{a} (-)^n \delta(y - b) - \cos \frac{m\pi x}{a} \delta(y) \right] [u(x) - u(x - a)] + \hat{y} \left[ \cos \frac{n\pi y}{b} \delta(x) - (-)^m \cos \frac{n\pi y}{b} \delta(x - a) \right] [u(y) - u(y - b)] \right\} \delta(z) . \quad (2.32)$$

The far field electric vector potential due to this single mode can be found from Eq. (2.26):

$$\vec{F}(r, \theta, \phi) = - \frac{te^{-jk_0 r}}{4\pi r} \left\{ \hat{x} \left[ (-)^n e^{jk_0 b \sin \theta \sin \phi} - 1 \right] \int_0^a \cos \frac{m\pi x}{a} e^{jk_0 x \sin \theta \cos \phi} dx + y \left[ 1 + (-)^{m+1} e^{jk_0 a \sin \theta \cos \phi} \right] \int_0^b \cos \frac{n\pi y}{b} e^{jk_0 y \sin \theta \sin \phi} dy \right\} . \quad (2.33)$$

Carrying out the integrations:

$$\vec{F}(r, \theta, \phi) = \frac{-jk_0 \sin \theta e^{-jk_0 r}}{2\pi r} \left\{ \frac{\left[ j(k_0 b \sin \theta \sin \phi - n\pi) - 1 \right] \left[ j(k_0 a \sin \theta \cos \phi - m\pi) - 1 \right]}{\left( \frac{m\pi}{a} \right)^2 - (k_0 \sin \theta \cos \phi)^2} \right. \\ \left. + \cos \phi - \frac{ye^{-jk_0 r}}{\left( \frac{n\pi}{b} \right)^2 - (k_0 \sin \theta \sin \phi)^2} \frac{\left[ j(k_0 a \sin \theta \cos \phi - m\pi) - 1 \right] \left[ j(k_0 b \sin \theta \sin \phi - n\pi) - 1 \right] \sin \phi}{\left( k_0 \sin \theta \sin \phi \right)^2} \right\} . \quad (2.34)$$

$$\vec{F}(r, \theta, \phi) = \frac{-2jk_0 te^{-jk_0 r}}{\pi r} \sin \theta \left\{ \frac{x \cos \phi}{(k_0 \sin \theta \cos \phi)^2 - \left( \frac{m\pi}{a} \right)^2} \right. \\ \left. - \frac{y \sin \phi}{(k_0 \sin \theta \sin \phi)^2 - \left( \frac{n\pi}{b} \right)^2} e^{j[k_0 (a \cos \phi + b \sin \phi) \sin \theta - (m+n)\pi/2]} \right. \\ \left. + \sin[(k_0 b \sin \theta \sin \phi - n\pi)/2] \sin[(k_0 a \sin \theta \cos \phi - m\pi)/2] \right\} . \quad (2.35)$$

Using superposition for all modes,  $\vec{F}$  due to the one amp current source at  $(x', y')$  is computed to be

$$\begin{aligned} \vec{F} &= \frac{2\omega_0 k_0 t e^{-jk_0 r}}{\pi r} \frac{\sin \theta}{ab} e^{jk_0 (a \cos \phi + b \sin \theta) \sin \theta} \\ &\cdot \sum_{m,n=0}^{\infty} \left\{ (-j)^{m+n} \sin[k_0 b \sin \theta \sin \phi - n\pi/2] \sin[(k_0 a \sin \theta \cos \phi - m\pi)/2] \right. \\ &\cdot \frac{\cos \frac{m\pi x'}{a} \cos \frac{n\pi y'}{b} j_0 \left( \frac{m\pi}{2} \frac{d}{a} \right)}{k^2 - k_{mn}^2} \\ &\cdot \left. \left[ \hat{x} \frac{\cos \phi}{(k_0 \sin \theta \cos \phi)^2 - \left( \frac{m\pi}{a} \right)^2} - \hat{y} \frac{\sin \phi}{(k_0 \sin \theta \sin \phi)^2 - \left( \frac{n\pi}{b} \right)^2} \right] \right\} . \quad (2.36) \end{aligned}$$

After finding the far field radiated power through the use of step 3, the radiated power  $P_r$  is computed:

$$P_r = 1/\eta_0 \int_{\phi=0}^{2\pi} \int_{\theta=0}^{\pi} \vec{E} \cdot \vec{E}^* r^2 \sin \theta d\phi \quad (2.37)$$

where \* denotes complex conjugate.

A quantity of great importance in the analysis of the antenna is  $Z$ , the antenna input impedance. The simplest method of computing this quantity would be to take the input impedance equal to the feed voltage since the feed current was assumed to be one amp.

$$Z = V/I = -t E_z \text{ (averaged over feed width)} = -\frac{t}{d} \int_{x' - \frac{d}{2}}^{x' + \frac{d}{2}} E_z dx . \quad (2.38)$$

One would not expect Eq. (2.38) to produce very accurate results since it takes no account of radiated power or power dissipated in the antenna structure if  $E_z$  is computed from Eq. (2.23) directly; this is found to be the case. Another

approach is to use the Poynting theorem to define input impedance. If a closed surface  $\Sigma$  is constructed in the far field of an antenna, where  $\Sigma$  encloses volume  $V$ , then the Poynting theorem gives the following result:

$$\begin{aligned} - \iiint_V \vec{E} \cdot \vec{J}^* dV &= \iint_{\Sigma} \vec{E} \times \vec{H}^* \cdot d\vec{S} + j\omega \iint_V \mu \vec{H} \cdot \vec{H}^* dV - j\omega \iint_V \epsilon \vec{E} \cdot \vec{E}^* dV \\ &\quad + \iint_V \sigma \vec{E} \cdot \vec{E}^* dV \end{aligned} \quad (2.39)$$

where  $d\vec{S}$  is the outward directed vector area element and  $dV$  is the volume element. Eq. (2.39) is often expressed in the following form:

$$VI^* = P_r + P_d + 2j\omega(W_m - W_e) \quad (2.40)$$

where  $VI^*$  is the complex power delivered to the antenna;  $P_r$  is the time-averaged radiated power;  $W_m$  and  $W_e$  are the time-averaged magnetic and electric stored energies, respectively, in  $V$ ; and  $P_d$  is the power dissipated in the antenna. For the microstrip antenna,  $P_d$  may be decomposed into two terms,  $P_c$  and  $P_d$ , representing the copper and dielectric loss, respectively. The stored energy and power terms are individually evaluated in the following.

In computing the electric and magnetic stored energies, the cavity model theory would assume that the bulk of the stored energy is contained in the interior region of the microstrip antenna. Therefore, these quantities are computed from the modal fields. The time-averaged electric stored energy is given by

$$W_e = (1/2) \epsilon \int_{x=0}^a \int_{y=0}^b |\vec{E}|^2 dy dx . \quad (2.41)$$

Writing this in terms of  $\psi_{mn}$ :

$$\mathcal{H}_e = (1/2) \omega^2 \mu_0^2 \frac{et}{ab} \sum_{m,n=0}^{\infty} \left| \frac{\psi_{mn}(x',y')}{k^2 - k_{mn}^2} \right|^2 j_0^2 \left( \frac{m\pi}{2} \frac{d}{a} \right) . \quad (2.42)$$

The time averaged magnetic stored energy is given by

$$W_m = (1/2) t \mu_0 \int_{x=0}^a \int_{y=0}^b |\vec{H}|^2 dx dy . \quad (2.43)$$

$\vec{H}$  may be written in terms of  $E_z$ :

$$W_m = (1/2) t \mu_0 \int_{x=0}^a \int_{y=0}^b \left| \frac{1}{j\omega\mu} \nabla E_z \right|^2 dy dx . \quad (2.44)$$

Finally, when  $E_z$  is expressed in terms of  $\psi_{mn}$ , one has

$$W_m = \frac{t}{2\omega^2 \mu_0} \sum_{m,n=0}^{\infty} j_0^2 \left( \frac{m\pi d}{2a} \right) \frac{\psi_{mn}^2(x',y')}{|k^2 - k_{mn}^2|^2} \int_{y=0}^b \int_{x=0}^a \nabla \psi_{mn} \cdot \nabla \psi_{mn} dx dy . \quad (2.45)$$

The integrand in Eq. (2.45) may be simplified by applying a vector identity derived in the next few equations. First,  $\nabla \cdot (\psi_{mn} \nabla \psi_{mn})$  is expanded.\*

$$\iint \nabla \psi_{mn} \cdot \nabla \psi_{mn} dx dy = \iint \nabla \cdot (\psi_{mn} \nabla \psi_{mn}) dx dy - \iint \psi_{mn} \nabla^2 \psi_{mn} dx dy . \quad (2.46)$$

---

\*The limits of double integrals in Eqs. (2.46) - (2.50) are understood to be  $x = 0$  to  $a$  and  $y = 0$  to  $b$ .

The two dimensional divergence theorem is now applied to the first integral on the right hand side of Eq. (2.46):

$$\iint \nabla \psi_{mn} \cdot \nabla \psi_{mn} dx dy = \oint_C \psi_{mn} \frac{\partial \psi_{mn}}{\partial n} dx - \iint \psi_{mn}^2 \psi_{mn} dx dy . \quad (2.47)$$

The line integral in Eq. (2.47) vanishes since  $\frac{\partial \psi_{mn}}{\partial n} \Big|_C = 0$ . The last integral on the right hand side of Eq. (2.47) is evaluated by noting that  $\nabla^2 \psi_{mn} = -k_{mn}^2 \psi_{mn}$ . Then, since the  $\psi_{mn}$  are normalized to unity, the result is

$$\iint \nabla \psi_{mn} \cdot \nabla \psi_{mn} dx dy = k_{mn}^2 . \quad (2.48)$$

Using Eq. (2.48), it is seen that the magnetic stored energy is

$$W_m = \frac{t}{2\epsilon_0^2 \mu_0} \sum_{m,n=0}^{\infty} \frac{k_{mn}^2 \psi_{mn}^2(x',y')}{|k^2 - k_{mn}^2|^2} j_0^2\left(\frac{m\pi d}{2a}\right) . \quad (2.49)$$

The power lost in the dielectric,  $P_d$ , is given by

$$P_d = t \omega \epsilon \delta \iint |E|^2 dx dy = 2\omega S W_e \quad (2.50)$$

where  $\delta$  is the loss tangent of the dielectric substrate.

The copper loss,  $P_c$ , is equal to twice the power lost in the metal patch element alone. The power dissipated in the patch can be found by the usual

perturbation method for good conductors. One first solves the problem for the ideal boundary condition  $\vec{z} \times \vec{E}|_{z=0^-} = 0$ . With this boundary condition enforced, one finds the surface current density on the underside of the patch  $\vec{J}_s = -\hat{z} \times \vec{H}|_{z=0^-}$ . Assuming that the actual copper coating is many skin depths deep (as it is in practical cases), one approximates  $\vec{J}$ , the actual current density in the copper, by

$$\vec{J} = \frac{1}{\Delta} \vec{J}_s e^{-z/\Delta} \quad (2.51)$$

where  $\Delta$  is the skin depth of the copper:

$$\Delta = \left( \frac{2}{\omega \mu_0 \sigma} \right)^{1/2} \quad (2.52)$$

This conduction current obeys Ohm's Law:  $\vec{J} = \sigma \vec{E}$ . The expression for the total copper loss (patch and groundplane) is found from Eq. (2.39).

$$P_c = \frac{2}{\sigma \Delta^2} \int_{x=0}^a \int_{y=0}^b \int_{z=0}^{\infty} |\vec{J}_s|^2 e^{-2z/\Delta} dz dy dx \quad . \quad (2.53)$$

$\vec{J}_s$  is now written in terms of  $\vec{H}$  and the integration with respect to  $z$  is carried out. Thus,

$$P_c = \frac{1}{\sigma \Delta} \iint_{\text{patch}} |\vec{H}|^2 dx dy \quad . \quad (2.54)$$

The above integral is proportional to the magnetic stored energy (2.43).

Therefore, the copper loss is

$$P_c = \frac{2}{\sigma t \mu_0 \Delta} W_m \quad . \quad (2.55)$$

Having computed the stored energy and loss terms, Eq. (2.40) is used to formulate two expressions for  $Z$ . First, since  $VI^* = ZII^*$ , one may write (remember that  $I = 1$  amp):

$$Z = P_r + P_d + P_c + 2j\omega(W_m - W_e) \quad . \quad (2.56)$$

Similarly,  $VI^* = VV^*/Z$ , which leads to the result

$$1/Z = [P_r + P_d + P_c - 2j\omega(W_m - W_e)]/|V|^2 \quad . \quad (2.57)$$

It is found that of the three formulations (2.38), (2.56), and (2.57), for input impedance, only Eq. (2.57) agrees with experimental measurements, and then only for frequencies near a strongly excited resonance. The explanation for this failure may be traced to the fact that the additional losses  $P_r$  and  $P_c$  are only partially accounted for in Eqs. (2.56) and (2.57) and not at all in Eq. (2.38), since  $\vec{E}$  (and therefore  $V$ ) as computed from (2.23) does not depend on these losses.

To rectify this problem, one may note that all thin microstrip antennas have so high a Q that the effects of all losses can be grouped together into a single "effective loss tangent,"  $\delta_{eff}$ . In doing so, the three formulas will then coincide, in fact, showing excellent agreement with measured results.

$\delta_{eff}$  is computed by noting that for an ideal cavity with lossless walls the loss tangent and the cavity quality factor are related by  $\delta = 1/Q$ . It is therefore reasonable to define  $\delta_{eff} = 1/Q = (P_r + P_c + P_d)/2\omega_0 W_e$ .  $\delta_{eff}$  is then used in place of  $\delta$  for all computations. Since all these power losses depend on  $E$  which in turn depends on  $\delta_{eff}$  as seen from Eq. (2.23), this definition thus leads to a complicated nonlinear equation for  $\delta_{eff}$ . It can be shown [5] that  $\delta_{eff}$  can be solved by an iterative procedure:

$$\delta_{i+1} = [P_r(\delta_i) + P_c(\delta_i) + P_d(\delta_i)]/2\omega_0 W_e(\delta_i)$$

where the starting value is  $\delta_0 = \delta$ . In practice, the value of  $\delta_{eff}$  is found to converge after a single iteration. In order to demonstrate the accuracy of the

theory, some typical results of measured and computed input impedances of a rectangular microstrip antenna are shown in Fig. 2.3. A rectangular microstrip antenna was constructed and fed through the ground plane by a semi-rigid coaxial cable at three successive points as shown in the figure. For each feed location, the impedance was measured at 5 MHz increments and plotted on a Smith chart as shown in Fig. 2.3b. To compute these loci via the theory, a value of  $d$  must be selected. In practice, the value found to give closest agreement between experiment and theory is used (about 3 to 4 times the diameter of the inner conductor). Note, however, that once  $d$  is determined for a single location and frequency, the same value yields accurate results for other frequencies and locations. When a microstrip feedline is used,  $d$  is the width of the line. Clearly the "effective feed width" is a problem deserving more investigation. Returning to Fig. 2.3, observe the excellent agreement between computed and measured loci. Thus, one may conclude that the theory provides a simple but very accurate prediction of microstrip antenna performance.

The last topic treated in this chapter is the formulation of an equivalent circuit model for the input impedance of a microstrip antenna when excited near resonance of one mode. Consider the input impedance of the antenna when fed again with a one amp source. For convenience, define  $k_{\text{eff}}^2 = k_0^2 \epsilon_r (1 - j \delta_{\text{eff}})$ . Then after performing the integration called for in Eq. (2.38), the expression for input impedance is

$$Z = j \omega_0 t \sum_{m,n=0}^{\infty} \frac{\psi_{mn}^2(x',y')}{k_{mn}^2 - k_{\text{eff}}^2} j_0^2\left(\frac{m\pi d}{2a}\right) . \quad (2.58)$$

Defining  $\omega_{mn} = ck_{mn}/\sqrt{\epsilon_r}$  where  $c = 3 \times 10^8$  m/s, Eq. (2.58) becomes

$$Z = \frac{j \omega_0 t c^2}{\epsilon_r} \sum_{m,n=0}^{\infty} \frac{\psi_{mn}^2(x',y')}{\omega_{mn}^2 - \omega^2(1 - j \delta_{\text{eff}})} j_0^2\left(\frac{m\pi d}{2a}\right) . \quad (2.59)$$

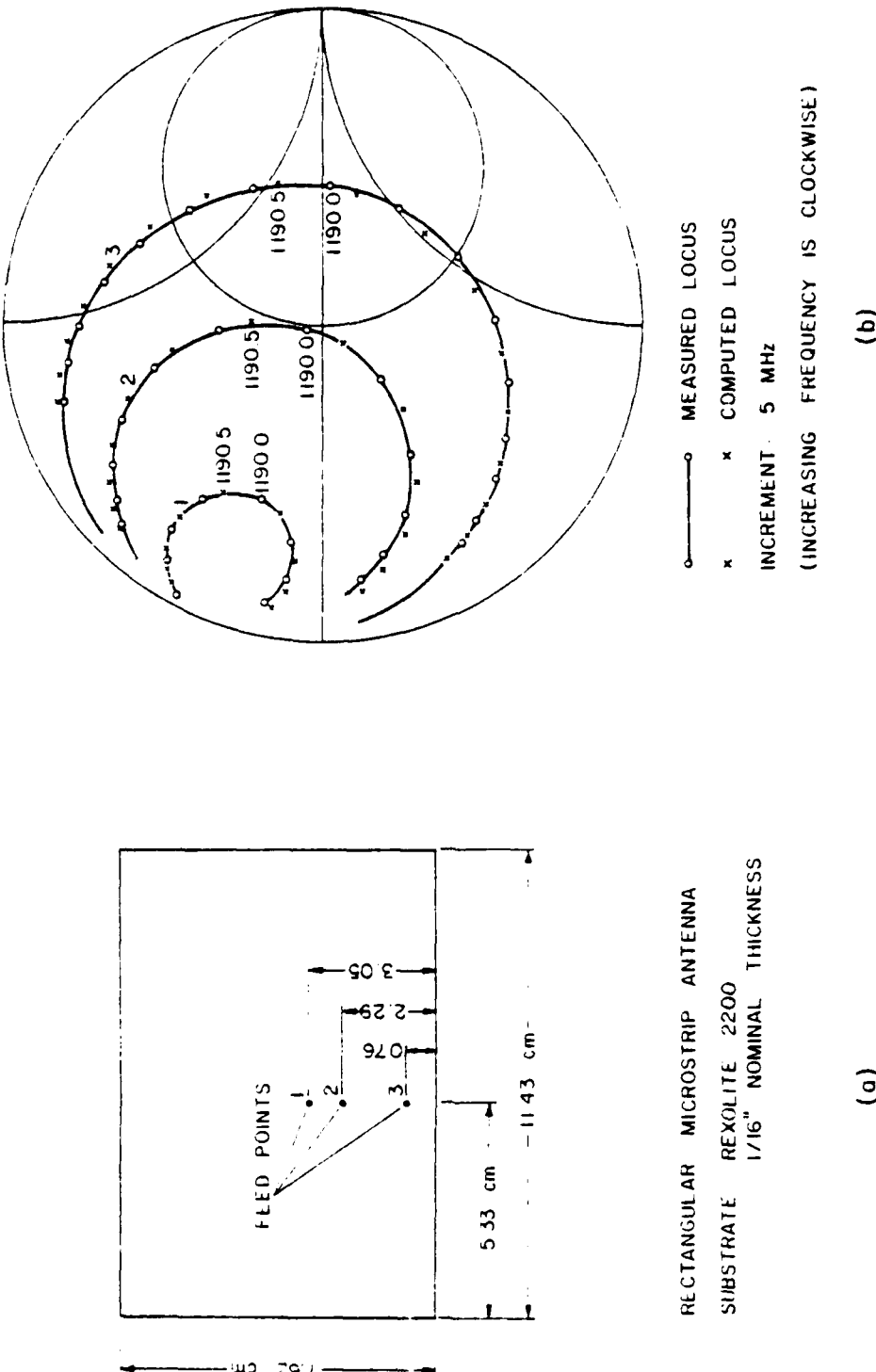


Figure 2.3. Impedance of a rectangular microstrip antenna. (a) Feed placement for impedance measurements; (b) Comparison of measured and computed impedance loci.

To simplify the appearance of Eq. (2.59), the quantity

$$\alpha_{mn} = \frac{\mu_0 tc^2}{\epsilon_r} \psi_{mn}^2(x', y') j_0^2\left(\frac{m\pi d}{2a}\right) \quad (2.60)$$

is defined. The input impedance can now be written as

$$Z = \sum_{m,n} \frac{\alpha_{mn}}{\omega \delta_{eff} + j\omega - j\frac{\omega_{mn}^2}{\omega}} \quad (2.61)$$

The form of the summand in Eq. (2.61) is suggestive of a parallel RLC resonant circuit. Therefore, the following definitions are made:

$$G_{mn}(\omega) = \omega \delta_{eff}/\alpha_{mn} \quad (2.62)$$

$$C_{mn} = 1/\alpha_{mn} \quad (2.63)$$

$$L_{mn} = \alpha_{mn}/\omega_{mn}^2 \quad (2.64)$$

Using these expressions, the expression for input impedance can now be written as

$$Z = \sum_{m,n=0}^{\infty} \frac{1}{G_{mn}(\omega) + j\omega C_{mn} - j1/\omega L_{mn}} \quad (2.65)$$

Typically, the microstrip radiators are very narrow band, in which case,  $G_{mn}(\omega)$  may be replaced by  $G_{mn}(\omega_{MN})$  for operation in the frequency band of mode  $(M,N)$ . Therefore, Eq. (2.65) represents a Foster expansion of the driving point impedance function. Since  $L_{mn}$  decreases with increasing modal indices, the infinite number of high order Foster sections can be simply combined to form a single series inductance, as illustrated in Fig. 2.4a.

In cases where the antenna is operating near a resonant frequency  $\omega_{MN}$  which is well separated from all other resonances, a simpler network formulation is possible. To demonstrate this, the  $MN$ th term is separated from the sum in Eq. (2.61) and the quantity  $(j\omega)$  is factored from the remaining terms.

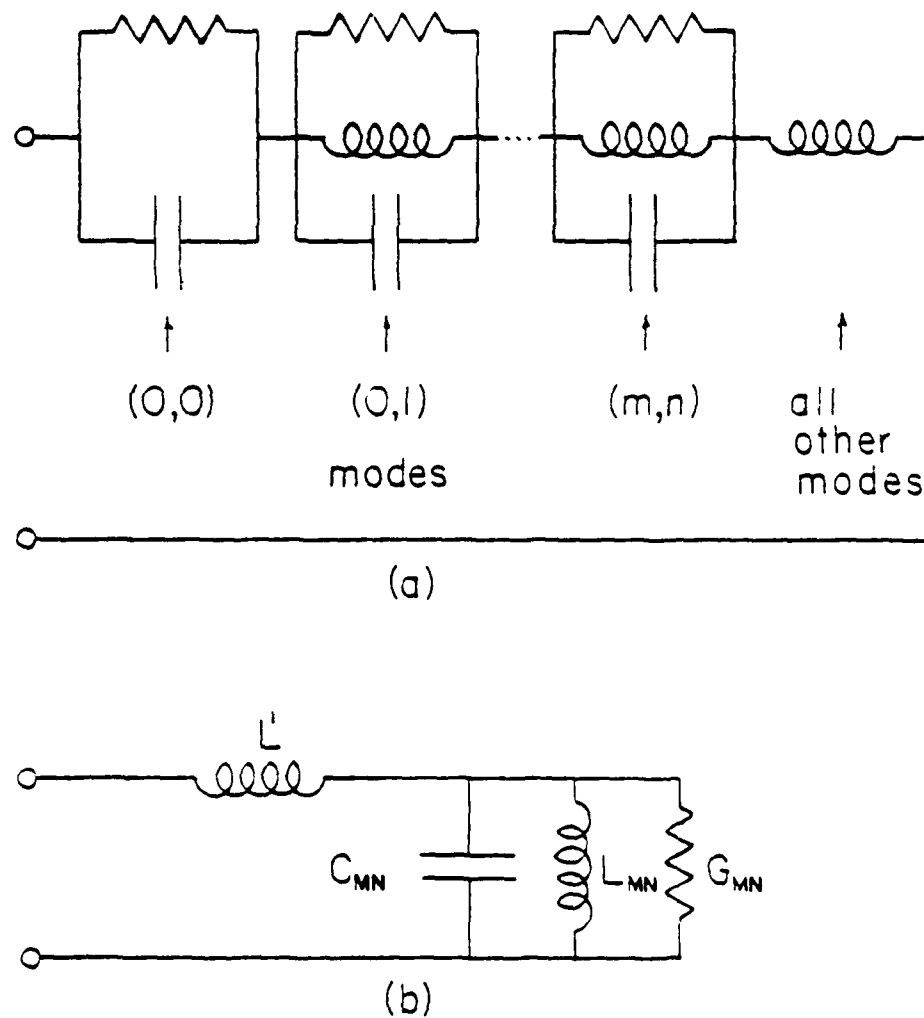


Figure 2.4. Circuit representations for microstrip antenna.  
 (a) Equivalent network for microstrip antenna;  
 (b) Equivalent network for excitation near an isolated mode.

$$Z = \frac{\alpha_{MN}}{\omega\delta_{eff} + j\omega - j\frac{\omega_{MN}}{\omega}} + j\omega \sum_{m,n \neq M,N} \frac{\alpha_{mn}}{\omega_{mn}^2 - \omega^2(1 - j\delta_{eff})}. \quad (2.66)$$

The first term on the right hand side of Eq. (2.66) may be replaced by the parameters of the Foster section for mode (M,N). The denominator of the summand may be replaced by  $\omega_{mn}^2 - \omega_{MN}^2$  since  $\omega^2 \approx \omega_{MN}^2$  and  $|\omega_{mn}^2 - \omega_{MN}^2|/\omega_{MN}^2 \gg \delta_{eff}$  for well separated modes. The result is

$$Z = \frac{1}{G_{MN}(\omega_{MN}) + j\omega C_{MN} - j\frac{1}{\omega L'_{MN}}} + j\omega L' \quad (2.67)$$

$$\text{where } L' = \sum_{m,n \neq M,N} \frac{\alpha_{mn}}{\omega_{mn}^2 - \omega_{MN}^2}.$$

The network model of the antenna operating near an isolated mode is therefore a parallel RLC circuit in series with a single inductance. This model is illustrated in Fig. 2.4b. The impedance locus is therefore a circle with center shifted into the inductive region as shown in Fig. 2.3.

In this chapter a simple cavity model for microstrip antennas has been described and has been developed in great detail for the case of a rectangular geometry. It was shown that the cavity theory can accurately predict the behavior of the antenna. A simple circuit model for the antenna was then developed as a logical extension to the theory. This circuit model provides one with a very simple means for the array design so far as the impedances and relative element currents and phases are concerned. A simple example will be considered later.

### III. CIRCULAR POLARIZATION IN MICROSTRIP ANTENNAS

Circular polarization (CP) in microstrip antennas arises due to the excitation of nearly degenerate modes. Two modes,  $\psi_{MN}$  and  $\psi_{M'N'}$ , are said to be degenerate when  $\omega_{MN} = \omega_{M'N'}$ , which implies, for the rectangular geometry,

$$\left(\frac{M}{a}\right)^2 + \left(\frac{N}{b}\right)^2 = \left(\frac{M'}{a}\right)^2 + \left(\frac{N'}{b}\right)^2 . \quad (3.1)$$

For the case of a square geometry,  $a = b$  and all modes are degenerate since  $\omega_{MN} = \omega_{NM}$ . Consider the behavior of the impedance as  $\omega \approx \omega_{MN} = \omega_{NM}$ . The series for  $Z$  in (2.58) will be dominated by the term

$$Z \approx \frac{D_{MN} + D_{NM}}{\omega_{MN}^2 - \omega^2 + j\omega^2 s_{eff}} \quad (3.2)$$

where

$$D_{MN} = \frac{j\omega t}{\epsilon_0 \epsilon_r} \psi_{MN}^2(x', y') j_0^2 \left( \frac{\pi d}{2a} \right) .$$

This term has the same form as in the case of well separated modes; thus, the locus of  $Z$  is expected, as observed, to be a circle on the Smith chart. However, if there is a slight imperfection in the construction so that  $a \neq b$ , the degenerate resonant frequency will split into two close ones. The corresponding modes will still be excited simultaneously as the frequency sweeps through their neighborhood, but the impedance locus will no longer be a circle. To see this, assume that  $\omega_{MN} < \omega_{NM}$ . Then

$$Z \approx \frac{D_{MN}}{\omega_{MN}^2 - \omega^2 + j\omega^2 s_{eff}} + \frac{D_{NM}}{\omega_{NM}^2 - \omega^2 + j\omega^2 s_{eff}} \quad \text{as } \omega < \omega_{MN} < \omega_{NM}$$

$$Z \approx \frac{D_{MN}}{\omega_{MN}^2 - \omega^2 - j\omega^2 s_{eff}} + \frac{D_{NM}}{\omega_{NM}^2 - \omega^2 + j\omega^2 s_{eff}} \quad \text{as } \omega_{MN} < \omega < \omega_{NM}$$

$$Z \approx -\frac{D_{MN}}{|i\omega_{MN}^2 - \omega^2| - j\omega_{eff}^2} - \frac{D_{NM}}{|i\omega_{NM}^2 - \omega^2| - j\omega_{eff}^2} \quad \text{as } \omega_{MN} < \omega < \omega_{NM}. \quad (3.3)$$

Now as the frequency sweeps through the two resonant frequencies, the impedance is seen to change drastically as  $\omega_{MN} < \omega < \omega_{NM}$ . This effect is seen as a cusp or small loop in the impedance locus as will be seen in Fig. 3.5.

For the nearly square antenna of Fig. 3.1a,  $a = b + c$  with  $c/b \ll 1$ , so that the resonant wave numbers  $k_{01}$  and  $k_{10}$  will be very close to one another. Feeding the antenna at point 1 will excite the  $\psi_{10}$  mode but not  $\psi_{01}$ . Feeding at point 3 will excite  $\psi_{01}$  but not  $\psi_{10}$ . Feeding at point 2, or on the diagonal through point 2, will excite both  $\psi_{01}$  and  $\psi_{10}$  modes, or a dominant field proportional to  $\psi_+ = \psi_{01} + \psi_{10}$ . With a feed at point 4, the excited field will be proportional to  $\psi_- = \psi_{01} - \psi_{10}$ . In the far field, in the direction perpendicular to the plane of the microstrip, the electric fields produced by  $\psi_{01}$  and  $\psi_{10}$  are polarized in the x and y directions, respectively, and can be written for the appropriate choice of input current magnitude and phase as

$$E_x \approx \frac{\cos(\pi x'/a)}{k_{eff}^2 - k_{01}^2}, \quad E_y \approx \frac{\cos(\pi y'/b)}{k_{eff}^2 - k_{10}^2}. \quad (3.4)$$

The contributions of the nonresonant modes are ignored in (3.4) for frequencies near the resonances of the two modes. To obtain CP in the direction of the zenith, the ratio of  $E_y$  to  $E_x$  should be  $\exp(\pm j\pi/2)$ . Define  $A = \cos(\pi y'/b)/\cos(\pi x'/a)$ . Then,

$$\frac{E_y}{E_x} \approx A \frac{k_{eff}^2 - k_{10}^2}{k_{eff}^2 - k_{01}^2} \approx A \frac{k - k_{10}}{k - k_{01}}. \quad (3.5)$$

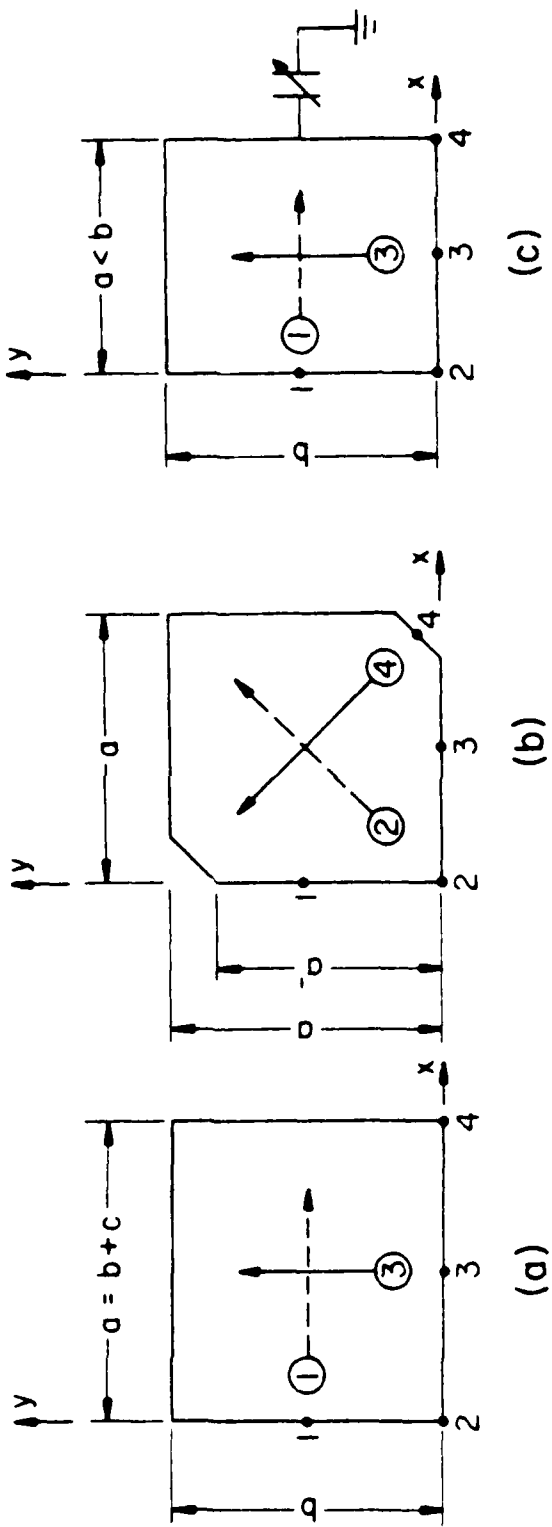


Fig. 3.1. Microstrip antennas capable of producing circular polarization

- (a) Nearly square microstrip.
- (b) Truncated microstrip.
- (c) Capacitively loaded microstrip.

Polarization of the far field in the  $\hat{z}$ -direction (zenith) is indicated by either a solid or a dashed arrow with a circled number corresponding to the feed location number.

It is particularly illuminating to plot  $k_{\text{eff}}$ ,  $k_{01}$ , and  $k_{10}$  in the complex  $k$  plane as was done in Fig. 3.2. For  $E_y/E_x$  to be  $\exp(j\pi/2)$ , Eq. (3.5) requires that

$$\Delta k = k_{01} - k_{10} = L(A + \frac{1}{A}) \quad . \quad (3.6)$$

Let  $k_{\text{eff}} = \bar{k} - jL$ ; then,

$$\frac{L}{\bar{k}} \approx \frac{1}{2} \quad ; \quad k_{\text{eff}} = \frac{1}{2Q} \quad . \quad (3.7a)$$

But

$$k_{01} - k_{10} = \frac{\pi}{b} - \frac{\pi}{a} = \frac{\pi}{b} - \frac{\pi}{b+c} \approx \frac{\pi c}{b^2} \quad , \quad (3.7b)$$

and

$$\bar{k}b \approx \pi \quad . \quad (3.7c)$$

Thus, combining (3.6) with (3.7), one obtains

$$\frac{\Delta k}{\bar{k}} = \frac{k_{01} - k_{10}}{\bar{k}} \approx \frac{c}{b} \approx \frac{A + (1/A)}{2Q} \quad . \quad (3.8)$$

For the case of the feed point taken on the diagonal of the microstrip,  $A = 1$  and, therefore,

$$\frac{a}{b} = 1 + 1/Q \quad . \quad (3.9)$$

This is an important formula, since it gives a simple means for determining the dimensions necessary for CP. The sense of the CP wave produced by the antenna when fed at point 2 will be left hand circularly polarized (right hand when fed at point 4). Fig. 3.3 shows the far field pattern of the nearly square antenna taken with a rotating dipole. The quality of the CP is very good broadside to the antenna and degrades to linear polarization on the horizon, as it must.

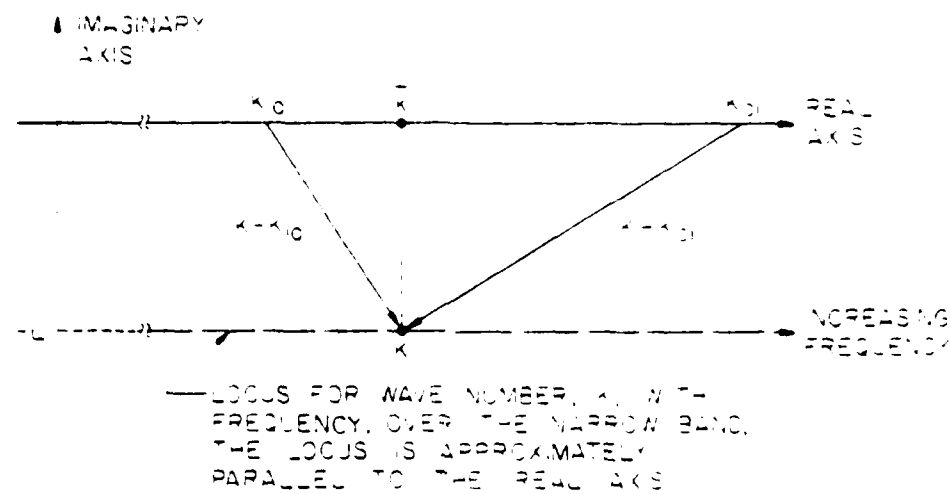


Fig. 3.2. Relative pole positions in the complex  $k$  plane.

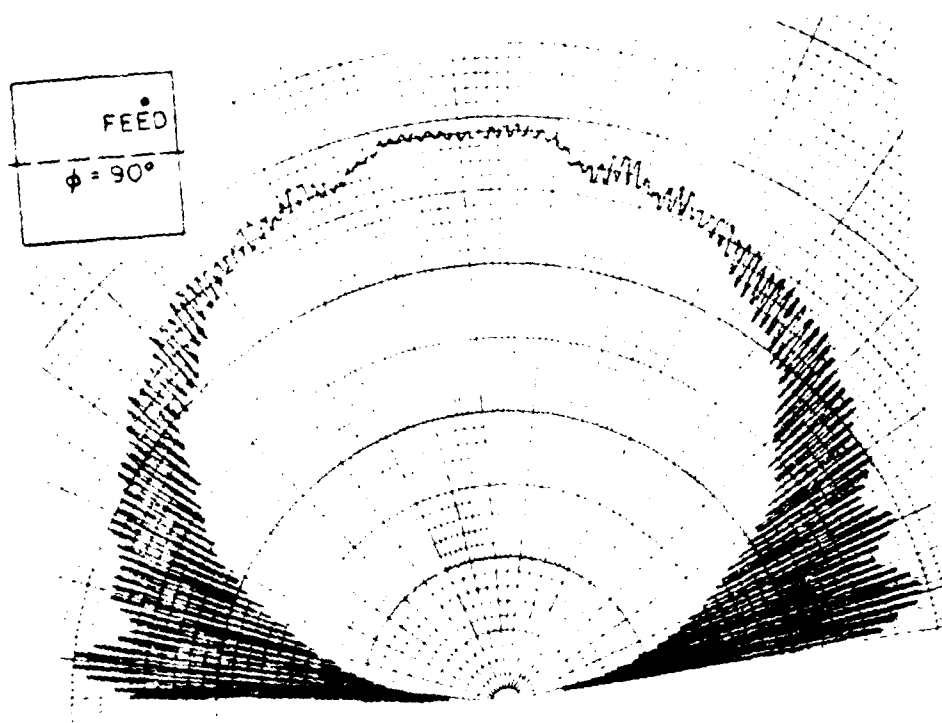
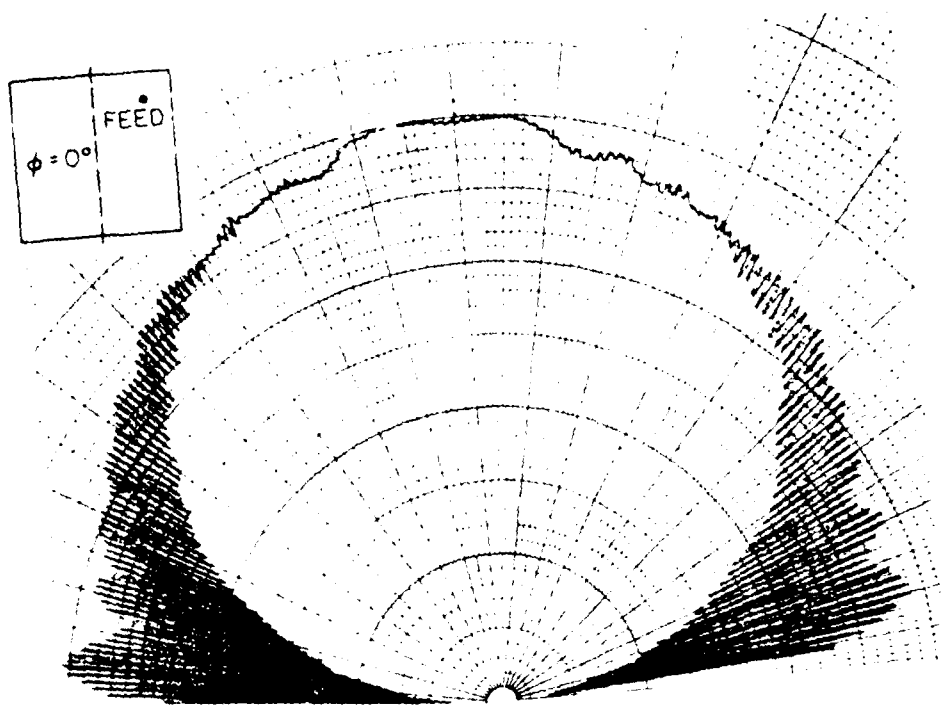


Fig. 10. Radiation patterns taken with rotating standard horn  
for two different feed positions of the parabolic antenna.

For the antenna of Fig. 3.1b, the analysis follows along the same lines as that for Fig. 3.1a. However, in this case, rather than  $\psi_{10}$  and  $\psi_{01}$ , modes  $\psi_+ = \psi_{01} + \psi_{10}$  and  $\psi_- = \psi_{01} - \psi_{10}$  are used, with corresponding wave numbers  $k_+$  and  $k_-$ . Of course, if the corners of the square microstrip are not trimmed off, the  $k_+ = k_-$ . However, by trimming the corners,  $k_-$  is increased while  $k_+$  remains almost unchanged. Obviously, if the opposite pair of corners were to be trimmed,  $k_+$  would increase and  $k_-$  would remain unchanged. The amount of shift in resonant frequency due to truncation of the corners has been estimated, using a perturbation formula [14], to be

$$\frac{k_- - k_+}{\bar{k}} \approx \frac{2(a - a')}{\pi a} \sin[\pi(a - a')/a]. \quad (3.10)$$

In order to test this prediction, an antenna was constructed from 1 oz copper-clad Rexolite 2200 with  $t = 1/16"$ ,  $a = 10.85$  cm, and  $a' = 10.29$  cm. To arrive at these dimensions, the Q of the square antenna was measured by feeding at point 1 of Fig. 3.1b. The corners were then trimmed until the percentage shift in resonant frequencies measured at points 2 and 4 equalled  $(100/Q)\%$  or 1% for this antenna according to Eq. (3.8). CP patterns similar to Fig. 3.3 were obtained. But using (3.10), one finds that a frequency shift of only 0.5% is predicted. This discrepancy is no unexpected, since Eq. (3.10) is based on the assumption that the boundary condition along the perimeter of the microstrip is that of a perfect magnetic wall. Although this assumption has proven reasonably applicable to the analysis of most aspects of microstrip antennas, it is not entirely adequate to predict the shift in poles in this critical application. It is believed that the complicated fringing fields at the corners where the perturbation formula is applied make the approximation insufficient. Note, however, that one can still rely on Eq. (3.8) for the required frequency

shift, and experimentally refine the proper dimensions by simply measuring the resonant frequencies corresponding to  $k_+$  and  $k_-$  by feeding at ports 2 and 4, respectively.

The antenna in Fig. 3.1c operates by the same mechanisms as that in Fig. 3.1a. In this case, however, the pole  $k_{10}$  can be varied by simply adjusting the capacitance attached to the antenna. (Since the capacitor is located at  $y = b/2$ , a null of the  $\psi_{01}$  mode,  $k_{01}$  is unaffected by the capacitor.) If the range of capacity is large enough, and  $a < b$ , one is able to adjust the antenna to produce fields of any polarization and sense. Thus, the antenna can be at one moment left hand CP, linear at the next, and right hand CP at some other time by simply changing the capacitance. However, since only one pole is affected by the capacitor, the frequency of operation shifts as the capacitance is varied. It should be noted that the capacitor could just as well have been located in the corner of the antenna in which case one would feed at points 1 or 3 to achieve CP operation.

Fig. 3.4 shows an exactly square microstrip antenna loaded by two independently biased varactor diodes. The varactors are located on nodal lines of the  $\psi_{10}$  and  $\psi_{01}$  modes. The biasing circuit arrangement shown in the figure ensures RF and DC isolation between the bias supplies and the antenna. The location of the varactors allows independent adjustment of the poles  $k_{01}$  and  $k_{10}$ . By this scheme, the difference in the poles  $k_{01} - k_{10}$  can be adjusted while keeping their mean,  $\bar{k}$ , fixed. Thus, for operation at a fixed frequency, virtually any polarization can be achieved simply by adjusting the varactor biases. Figures 3.5 and 3.6 show the impedance and radiation patterns of this antenna for the various polarizations. The patterns were taken with LH and RH CP antennas. The asymmetry in the patterns is probably due to the asymmetrical placement of the

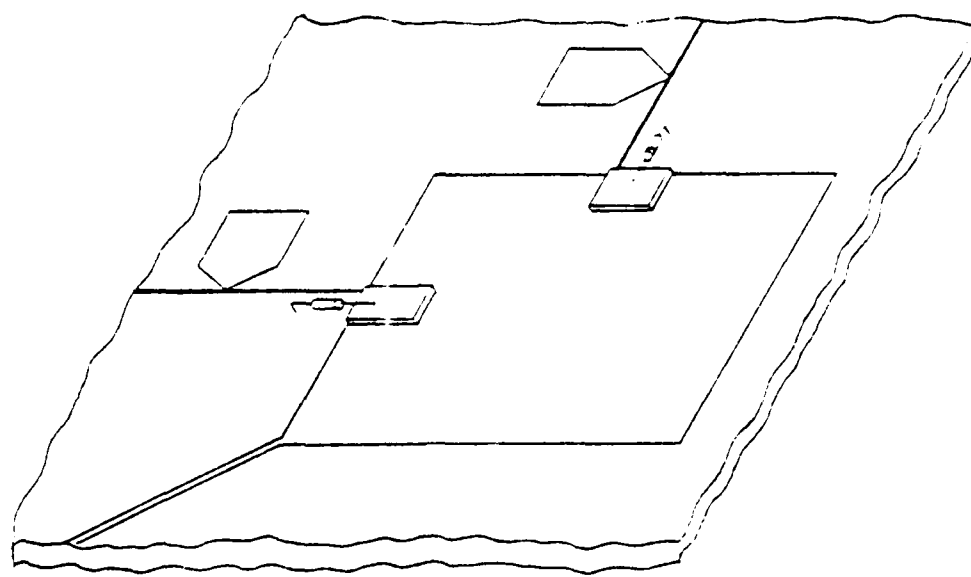


Fig. 3.4a. Double tuned antenna.

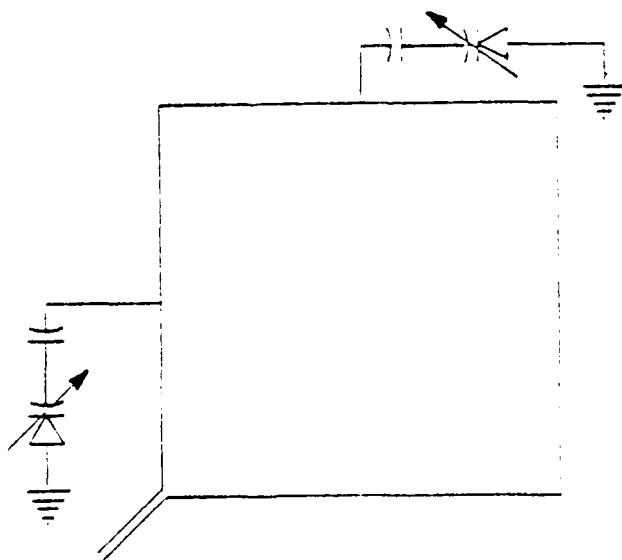


Fig. 3.4b. Double tuned antenna schematic.

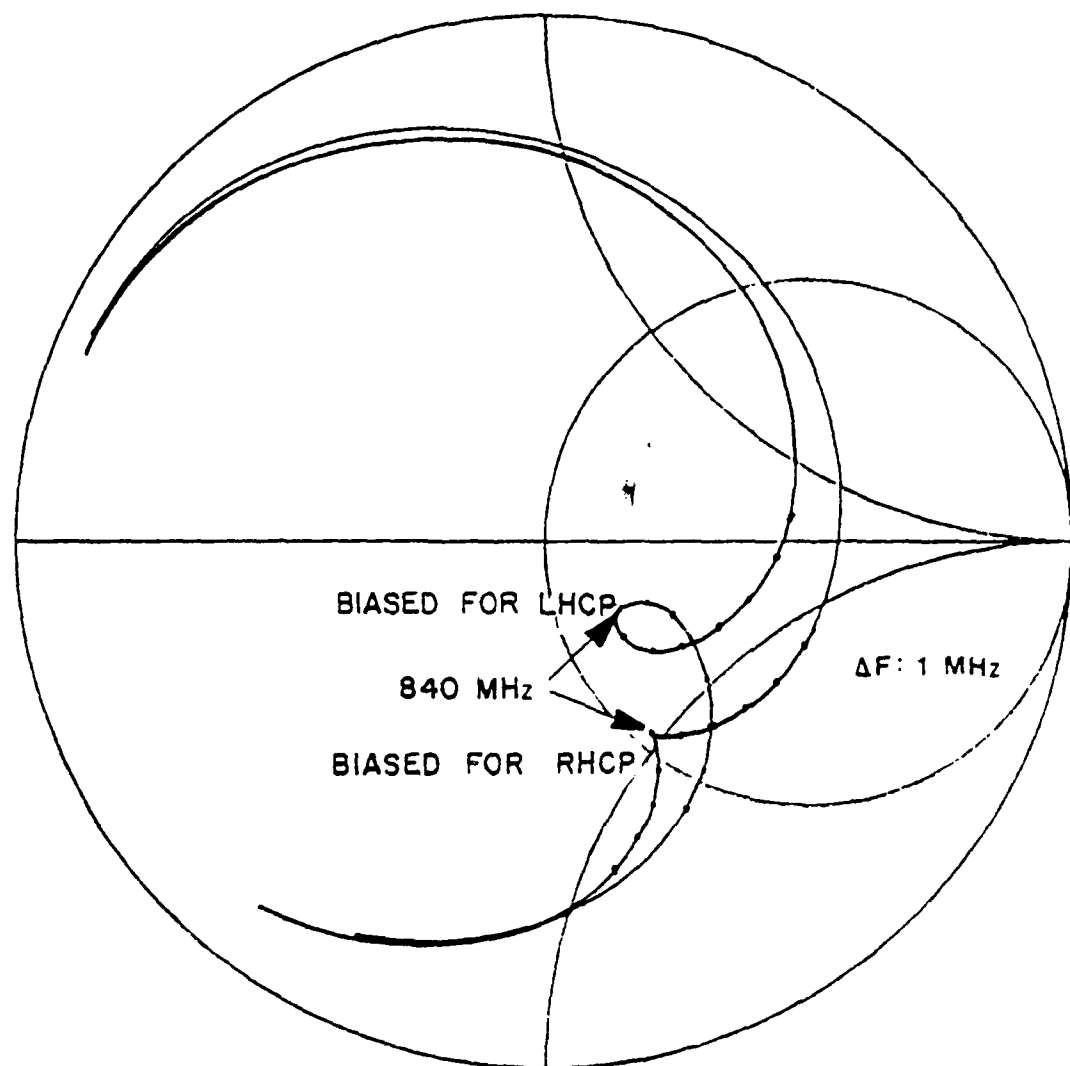


Fig. 3.5. Impedance of double tuned antenna.

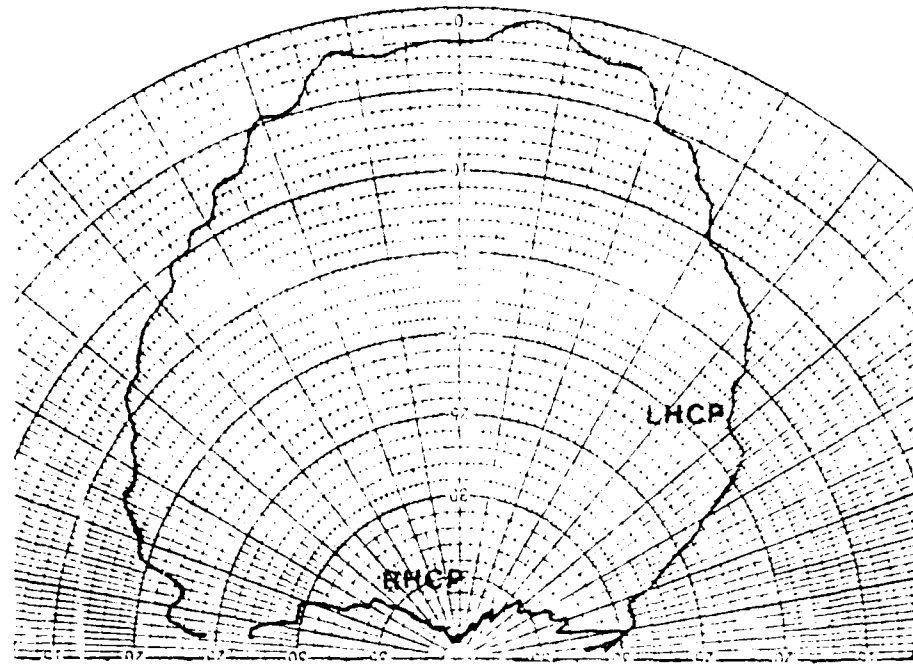


Fig. 3.6a. Left and right hand CP patterns of double tuned antenna biased for LHCP.

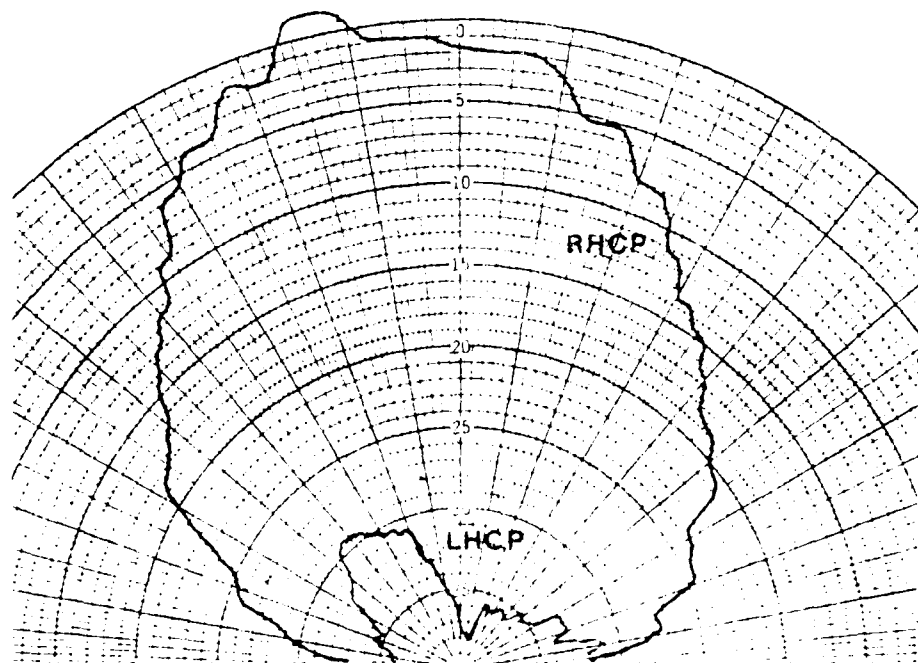


Fig. 3.6b. Left and right hand CP patterns of double tuned antenna biased for RHCP.

diodes. It is conjectured that using two pairs of matched diodes on opposite sides of the antenna would minimize this effect.

Using the double-tuned antenna of Fig. 3.4, it is also possible to vary the frequency of operation without interfering with the state of polarization. The double-tuned antenna constructed is tunable from 800 MHz to 340 MHz while still maintaining quite good CP. Obviously, the tuning bandwidth is dependent on the quality of varactors used.

Other single-feed CP microstrip antennas can be explained in the same way as the rectangular. A disk microstrip antenna was designed on the basis of this theory. A capacitor to the ground plane was attached to the circumference of the disk. When fed at an angle of forty-five degrees from the capacitor, CP operation was also obtained.

Although all these antennas are able to produce good CP without the need of an external phase-shifter and power divider, a distinct advantage, it is clear from the theory given above that their CP operation is extremely narrow band. Fig. 3.7 shows the predicted degradation in axial ratio with normalized frequency defined as

$$\xi = \frac{k - \bar{k}}{k_{01} - k_{10}} . \quad (3.11)$$

Thus, for an axial ratio within 3 dB (at zenith), which would produce a polarization mismatch loss of less than 1/4 dB with respect to CP, one is limited, for 1/16" Rexolite 2200 at about 800 MHz, to a bandwidth of about 35% of the frequency difference between the two dominant poles or about (35/Q) percent bandwidth. Fig. 3.7 applies to any CP microstrip whose feed excites both of the nearly degenerate modes equally. The close agreement between theory and experiment is shown in Fig. 3.8, where axial ratio as a function of frequency is plotted for the nearly square antenna.

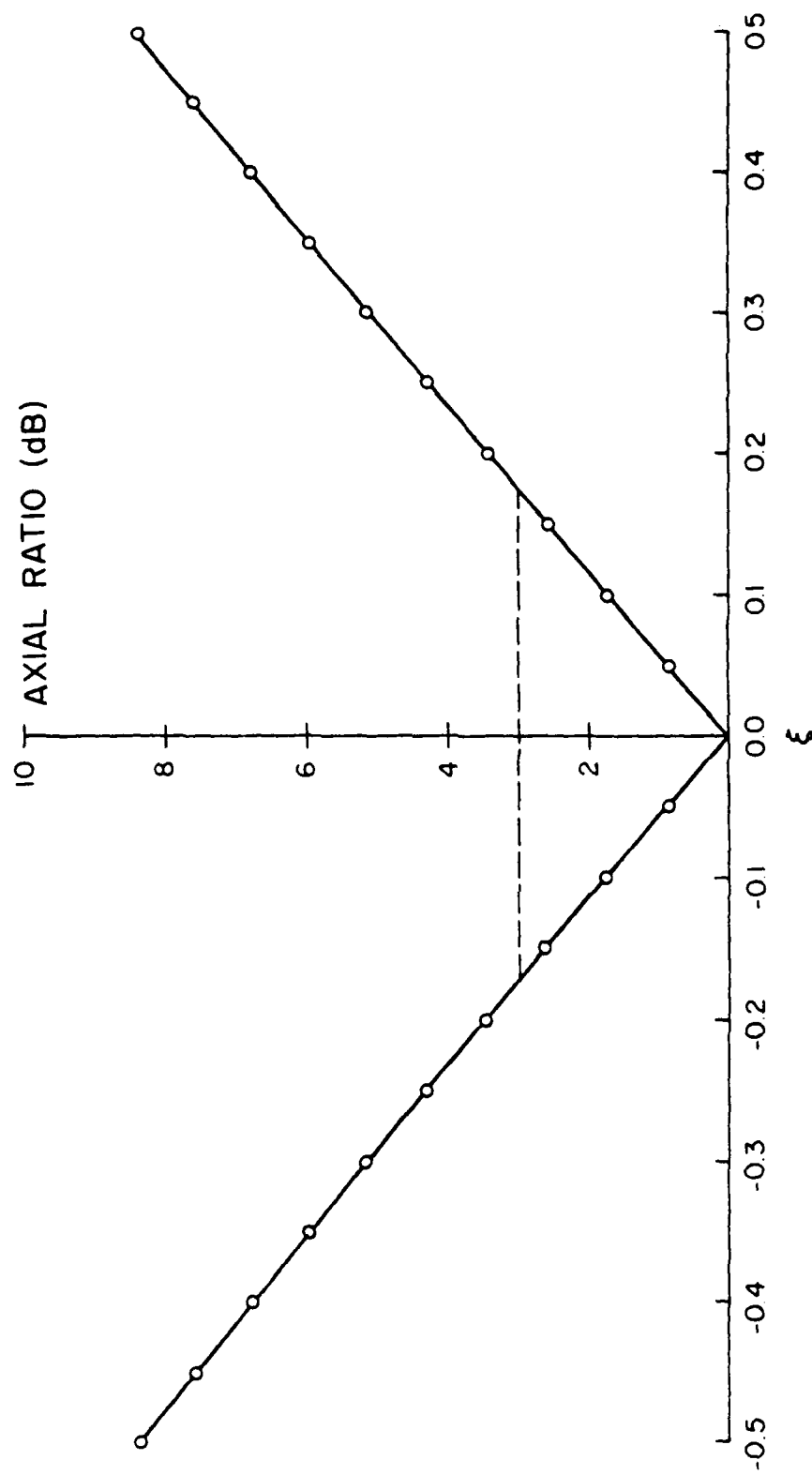


fig. 3.7. Degradation of axial ratio with normalized frequency.

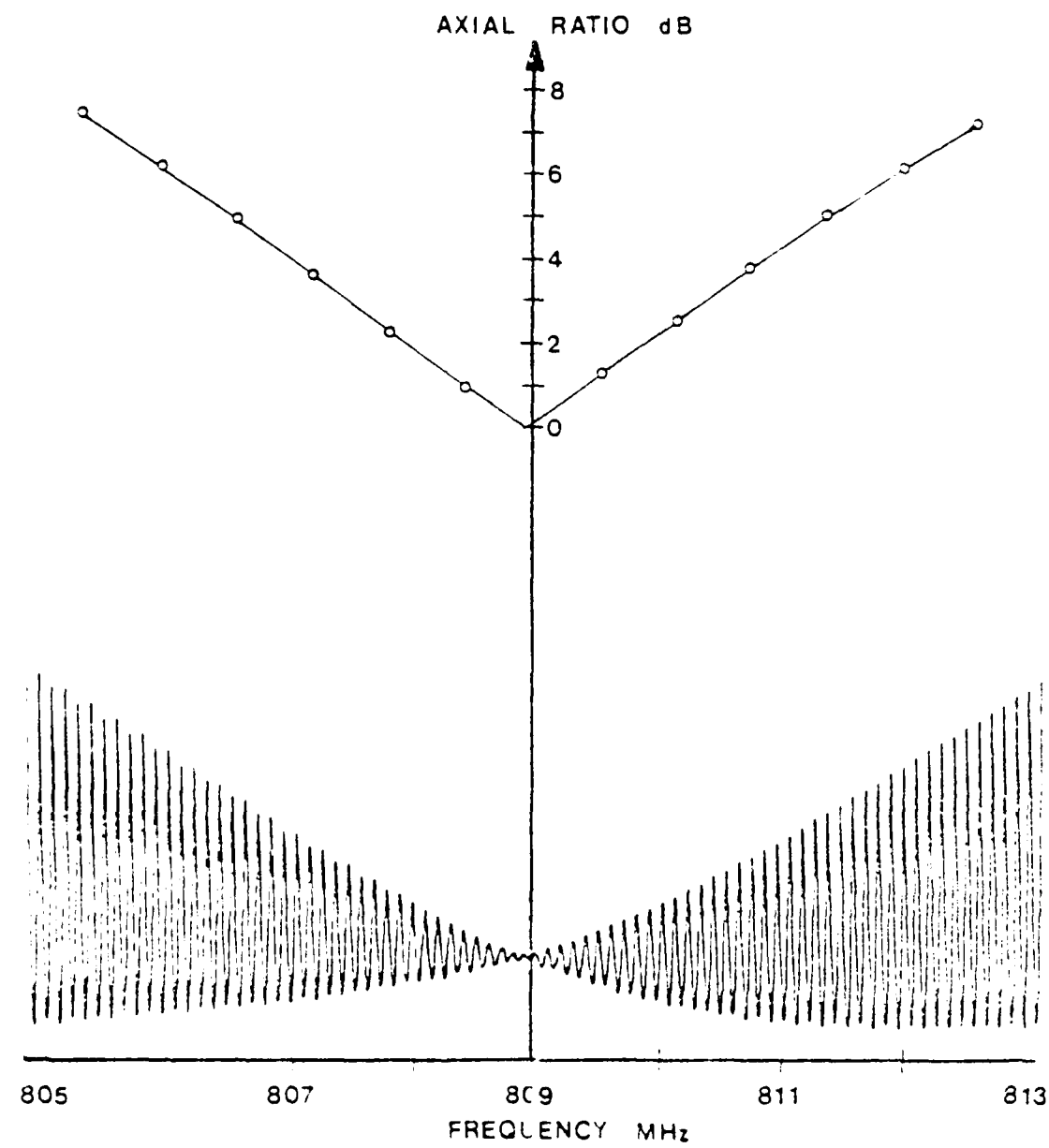


Fig. 3.3. Measured response of rotating dipole and plot of axial ratio for nearly square antenna.

In this chapter the mechanism characterizing the operation of singly fed CP microstrip antennas has been described in a simple and useful manner. For geometries for which the difference in the resonant frequencies of the two nearly degenerate modes can be computed with sufficient accuracy (such as rectangular or elliptical patches), the exact dimensions can be successfully calculated by knowing the Q of the antenna. For perturbed patches that lead to nonseparable geometries, one can fairly quickly determine the dimensions without making tedious pattern measurements by adjusting the pole location such that  $\Delta k/k = 1/Q$ . Finally, a curve has been plotted which allows one to quickly predict the pattern bandwidth of the CP antenna.

#### IV. CHARACTERIZATION OF THE MICROSTRIP LINE AND COAXIAL TRANSITION

When a microstrip antenna is fed with a microstrip line, it becomes a monolithic device, which can easily be fabricated and reproduced simply by a printed-circuit technique. But in this case, the antenna must be fed through the perimeter of the patch, thus losing the flexibility of the coaxial feed which can be located in the patch for certain desired impedance and polarization characteristics. Furthermore, in general, the strip line will eventually be connected to a source (or receiver) through a coaxial transition. This is indeed the case in most measurement systems, if not all. For this reason, an investigation of the strip line-to-coax transition is of interest in its own right.

In our study of arrays to be discussed in the next chapter, some inconsistencies were observed in the measured results through different ways, and thus caused difficulties in formulating a theoretical design procedure for the array. In an attempt to trace the source of the inconsistency, each part in the array was investigated in great detail. In so doing, we were confronted with the interesting question: how to determine the s-parameters of a small discontinuity accurately. It is found that extreme care must be exercised in the procedure of measurement; otherwise, ridiculous values of the s-parameters may likely result. For this reason, it is also necessary to investigate the characteristics of the strip line-to-coax connector discontinuity.

In this chapter, the techniques used to model microstrip lines to coaxial cable connectors are presented. First consider a mirostrip line which consists of a ground plane, a dielectric sheet of thickness  $t$ , and a metal strip conductor of width  $w$ , as illustrated in Fig. 4.1. The quantities of interest

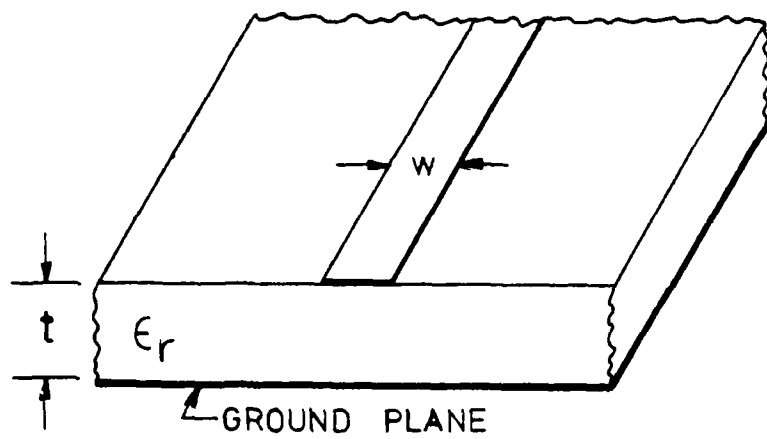


Fig. 4.1. The microstrip transmission line.

associated with the line are  $Z_0$ , the characteristic impedance of the line,  $v_p$ , the phase velocity in the line, and  $\alpha$ , the attenuation constant of the line. A useful analysis of the line will predict these quantities.

Because the field lines between the strip and the ground plane are not contained entirely within the dielectric substrate, the propagating wave along the line is not purely transverse electromagnetic (TEM). However, for low enough frequencies of operation the fields are nearly transverse and the propagating mode may be characterized by an "effective dielectric constant,"  $\epsilon_e$ , which is defined by the relation

$$v_p = \frac{v_0}{\sqrt{\epsilon_e}} \quad (4.1)$$

where  $v_0 = (\mu_0 \epsilon_0)^{-1/2}$ . This "quasi-TEM" mode is a useful concept for frequencies where the longitudinal component of the field is negligible compared to the transverse component.

Several methods have been reported in the literature for determining  $\epsilon_e$  and  $Z_0$ . These include conformal mapping [15], variational techniques [16], and the method of Green's functions [17]. For the purposes of this report, closed form expressions suitable for computer-aided design were sought. Hammerstad [18] has reported closed form expressions accurate to within 1% relative error for values of  $\epsilon_e$  and  $Z_0$  commonly obtained:

$$\epsilon_e = \frac{\epsilon_r + 1}{2} + \frac{\epsilon_r - 1}{2} (1 + 12t/w)^{-1/2} + K \quad (4.2)$$

where

$$K = \begin{cases} 0.04(1 - w/t)^2 & \text{for } w/t \leq 1 \\ 0 & \text{for } w/t > 1 \end{cases}$$

$$Z_0 = \begin{cases} \left( \frac{\epsilon_0}{\epsilon_0 \epsilon_r} \right)^{1/2} \cdot \frac{1}{2} \cdot \ln(8t/w + 0.25) & \text{for } w/t \leq 1 \\ \left( \frac{\epsilon_0}{\epsilon_0 \epsilon_r} \right)^{1/2} \cdot \frac{1}{w/t + 1.393 + 0.667 \cdot \ln(w/t + 1.444)} & \text{for } w/t > 1 \end{cases} \quad (4.3)$$

It is possible to take the finite thickness,  $t$ , of the strip conductor into account by introducing an effective strip width  $w_e$ ; however, for the 1 mil thick copper-clad Rexolite sheets used in this report, the correction is not necessary.

There are two sources of dissipative loss in a microstrip line: conductor loss and substrate dielectric loss. Pucel [19] has reported very accurate expressions for  $\alpha_c$ , the conductor loss factor:

$$\alpha_c = \begin{cases} \frac{R_s}{2\pi Z_0 t} \cdot P \cdot \left[ 1 + t/W + t/\pi W \cdot \left( \ln \frac{(4-W)}{W} + \frac{2}{W} \right) \right], & \text{for } W/t \leq 1/2 \\ \frac{R_s}{2\pi Z_0 t} \cdot P \cdot Q, & \text{for } 1/2 \leq W/t \leq 2 \\ \frac{R_s}{Z_0 t} \cdot Q \cdot \left( \frac{W}{t} + \frac{2}{\pi} \ln(2) \exp(W/2t + 0.94) \right)^{-2} \cdot \frac{W}{t} + \frac{W/(-t)}{(W/2t) + 0.94}, & \text{for } W/t \geq 2 \end{cases} \quad (4.4)$$

where

$$R_s = \left( \frac{\epsilon_0}{2\pi} \right)^{1/2}$$

$$P = 1 - (W/4t)^2$$

$$Q = 1 + t/W + t/\pi W \left( -\frac{2t}{\pi} - \frac{2}{t} \right).$$

Schneider [20] derived the following expression for  $\alpha_d$ , the dielectric loss factor:

$$\alpha_d = \frac{\pi^2 c}{\lambda^2} \cdot \frac{e^{-\gamma}}{r^{1/2}} \cdot \frac{1}{(1 - \beta)} \quad (4.5)$$

where  $\lambda$  is the free space wavelength. The total loss factor,  $\beta$ , is the sum of  $\beta_R$  and  $\beta_{LR}$ .

An experiment was performed in order to test the validity of the above equations. A microstrip line with  $w = 0.44$  cm and  $t = 0.16$  cm was constructed. The microstrip line was terminated with an open circuit located a distance  $d$  from the feed point. The magnitude and phase of  $\Gamma_0$ , the voltage reflection coefficient, was measured for various values of  $d$  using an HP 4010A network analyzer, HP 8632A sweep generator, HP 8444 polar display, and HP 8745A  $S$ -parameter test set. According to the simple transmission line theory, the measured reflection coefficient should be

$$|\Gamma_0| = |\Gamma| e^{-\gamma(d-d_0)} e^{-j\phi(d-d_0)} = e^{-2\gamma(d-d_0)} e^{-j2\phi(d-d_0)} \quad (4.6)$$

where  $\gamma = jk_0/\sqrt{\epsilon_r - 1}$  is the propagation constant of the line. Thus, the simple transmission line theory predicts linear phase progression and exponentially decreasing magnitude of  $|\Gamma_0|$  with distance  $d$ . The measured values of return loss,  $R$ , and  $\text{Ang}$  are shown in Fig. 4.2a. Return loss is expressed in dB, as defined by,

$$R = -10 \log_{10} |\Gamma_0|^2 \quad (4.7)$$

From the phase plot, the measured value of  $\gamma$  is found to be  $0.203 \text{ cm}^{-1}$ , which agrees quite well with the value of  $0.147 \text{ cm}^{-1}$  predicted using Eq. (4.2). However, the return loss plot in Fig. 4.2b shows an unexplained oscillatory behavior. In order to find the cause of this oscillatory, a closer inspection of the experimental procedure is necessary.

The often necessary determination of the reactance at the end of the line due to bonding effects, is not the effect in question for each measurement. However,

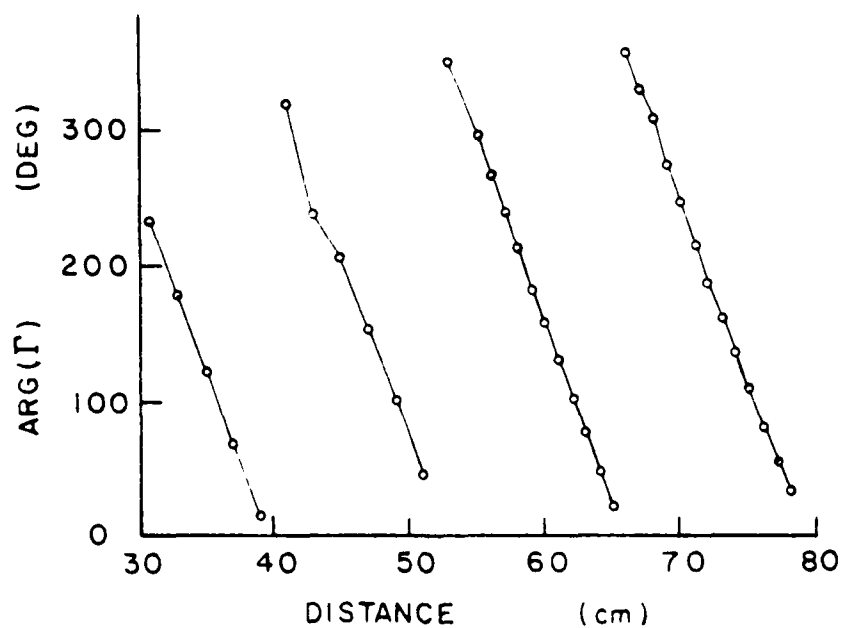
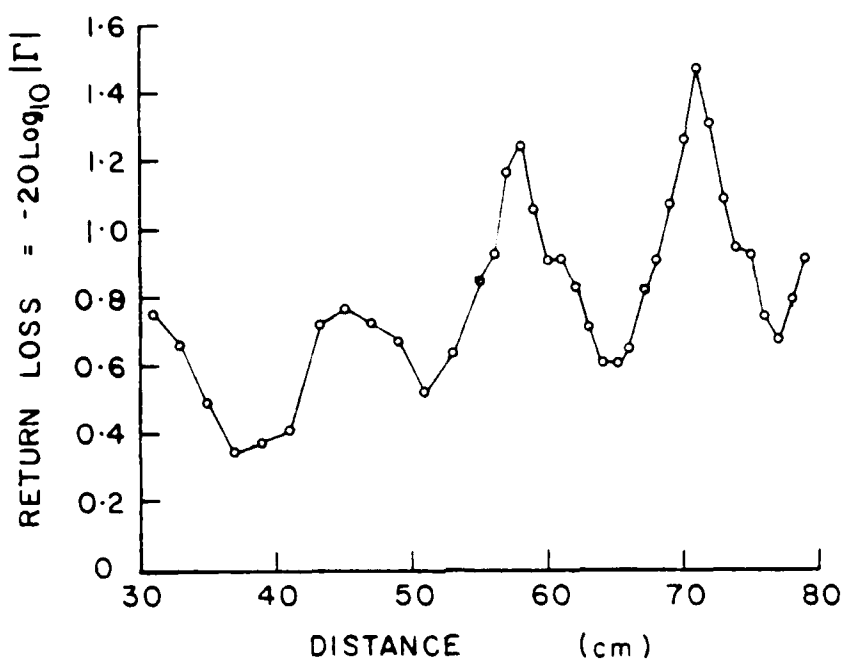


Fig. 4.2. Measured return loss and phase of  $\Gamma$ , the voltage reflection coefficient, versus distance from open-circuited end of a microstrip fifty ohm line at 800 MHz.

the transition between the coaxial cable and the microstrip line is effected by a "launching" device which has imperfect matching properties. Therefore, multiple reflections between the "launcher" and the open circuit may explain why the return loss plot shows periodic oscillations with d.

Consider the "launcher" to be a two-port device, with port 1 connected to the coaxial cable and the microstrip connection designated as port 2. Using these definitions, the reflection coefficient,  $\Gamma'$ , measured at port 1 will be related to  $\Gamma$ , the actual reflection coefficient in the microstrip line at port 2, by

$$\Gamma' = S_{11} + \frac{S_{12}S_{21}^T}{1 - S_{22}^T} \quad (4.8)$$

where the  $\{S_{ij}\}$  are the two port scattering parameters which characterize the junction. It is reasonable to assume that the "launcher" is a reciprocal device, in which case  $S_{12} = S_{21}$ . Also, if the device is nearly lossless, then  $|S_{11}| \approx |S_{22}|$ . To see how the oscillations in Fig. 4.2b can come about, assume that the connector provides a "good" transition, i.e.,  $|S_{11}| \ll 1$ , and  $|S_{12}| \approx 1$ . Then the expression for return loss is approximately given by

$$R = -20\log_{10}|\Gamma'| \approx -40\log_{10}S_{12} + \frac{20}{\ln 10}(2\pi d) - \frac{20}{\ln 10}|S_{22}|e^{-2\pi d} \cdot \cos(\text{Arg}S_{22} - 2\pi d) \quad (4.9)$$

It is now seen from Equation (4.9) that the plot of R versus d will be an exponentially decreasing sinusoid superimposed on a straight line. Thus, the slope of the line fitted to the data by the method of least squares should provide a value for  $\lambda$ . The value of  $\lambda$  so obtained from the data of Fig. 4.2a is  $0.0006 \text{ cm}^{-1}$  which agrees fairly well with  $0.0003 \text{ cm}^{-1}$ , the value obtained from Equations (4.1) and (4.5).

At this point a discussion of the types of microstrip to coaxial transitions is in order. Several types of backwall launchers are shown in Figs. 4.3 and 4.4. These backwall launchers are convenient because the groundplane acts as a shield, preventing the presence of the connecting hardware from disturbing the microstrip operation. Fig. 4.3 shows an SMA semi-rigid coaxial connector and Fig. 4.4 illustrates an n-type coaxial transition. Due to mechanical considerations, the connector of Fig. 4.4 was used exclusively for the parameter work in this report.

In order to uniquely define the scattering parameters of the device, junction planes which demarcate the device boundaries must be defined. The junction plane for port 1 is defined to coincide with the bottom face of the Teflon sheath surrounding the center conductor. The junction plane for port 2 cuts the microstrip line at the position of the center conductor screw. The problem of determining the scattering parameters of a small discontinuity can be quite difficult, since given several values of  $\Gamma$ , there are many possible combinations of the  $\{S_{ij}\}$  which will give nearly the same value of  $\Gamma$ . The classical method [21] for measuring the scattering parameter of a 2-port through a line consists of an experiment similar to the one described above, with  $\beta d = 0, \pi/4, \pi/2$ , and  $3\pi/4$ . The scattering parameters are then determined by graphical means on the Smith chart. For example,  $S_{11}$  is the point lying at the center of the circle on which the four measured values of  $\Gamma$  fall. However, the method must be modified for the present case. When the discontinuity presented by the two-port is small, the four points will lie on a circle of large radius, that is, near the edge of the Smith chart. It is then difficult to determine  $S_{11}$  accurately. In order to do so, it would be desirable for  $|\Gamma|$  to be small so that  $\Gamma$  is essentially equal to  $S_{11}$ . However,

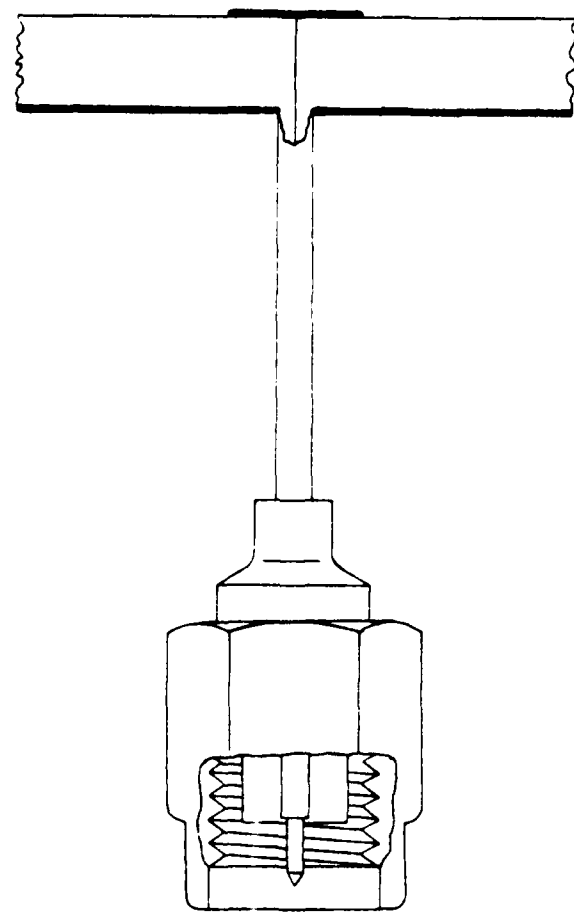


Fig. 4.3. SMA semi-rigid coaxial transition.

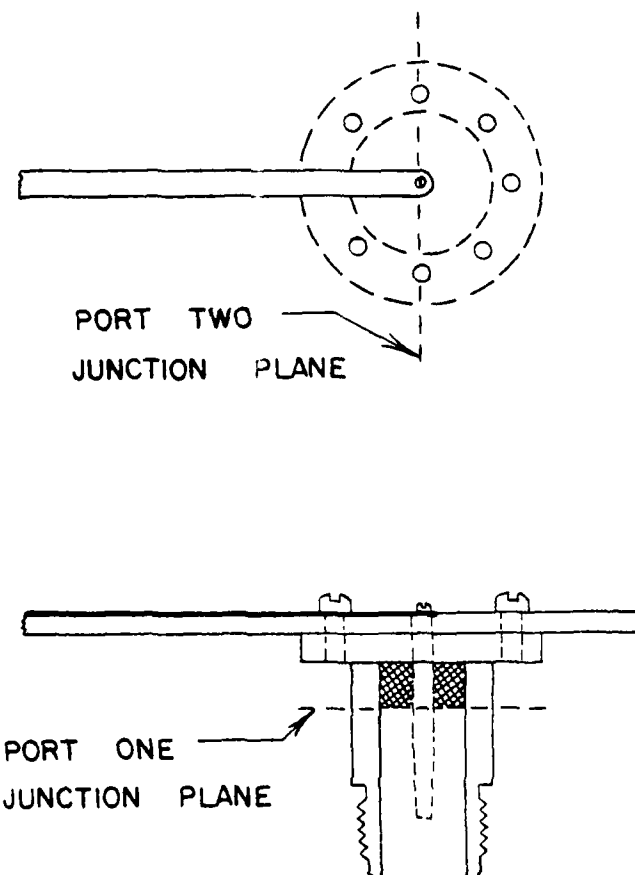


Fig. 4.4. Type II coaxial transition.

in order to measure  $S_{12}$ , a large value of  $|T_1|$  is desired. Thus, the following experimental procedure is suggested.

Using Equation (4.3) for dimensions, a nominal 50Ω microstrip line is constructed, terminated at each end by identical n-type transitions. Measurements of the reflection coefficient are made at one port while the opposite port is successively match-terminated and short circuit-terminated. These measurements are repeated while the length,  $d$ , of the connecting line is varied. The experimental setup is sketched in Fig. 4.5. Using the notation of the figure, the following relations are simply derived.

$$\Gamma = \begin{cases} 0 & \text{for } Z_2 = 50\Omega \\ -1 & \text{for } Z_2 = 0\Omega \end{cases} \quad (4.10a)$$

$$\Gamma' = S_{22} + \frac{S_{12}^2}{1 - S_{11}} \quad (4.10b)$$

$$\Gamma'' = e^{-j2\beta d} e^{-2\alpha d} \Gamma' \quad (4.10c)$$

$$\Gamma''' = S_{11} + \frac{S_{12}^2 \Gamma''}{1 - S_{22} \Gamma''}. \quad (4.10d)$$

When the output port is matched, we have

$$\Gamma''' = S_{11} + \frac{S_{12}^2 (e^{-2j\beta d} e^{-2\alpha d} S_{22})}{1 - S_{22}^2 e^{-2j\beta d} e^{-2\alpha d}} \approx S_{11} + S_{12}^2 S_{22} e^{-2j\beta d} e^{-2\alpha d}. \quad (4.11)$$

For small losses, Equation (4.11) is the parametric equation of a circle in the  $\Gamma'''$  plane with center at  $S_{11}$ . Thus, by varying  $d$ ,  $\Gamma'''$  will move on a circle centered at  $S_{11}$  of radius  $|S_{12}^2 S_{22}|^{1/2}$ . The experimental data from this experiment performed at 800 MHz are plotted on the Smith chart in

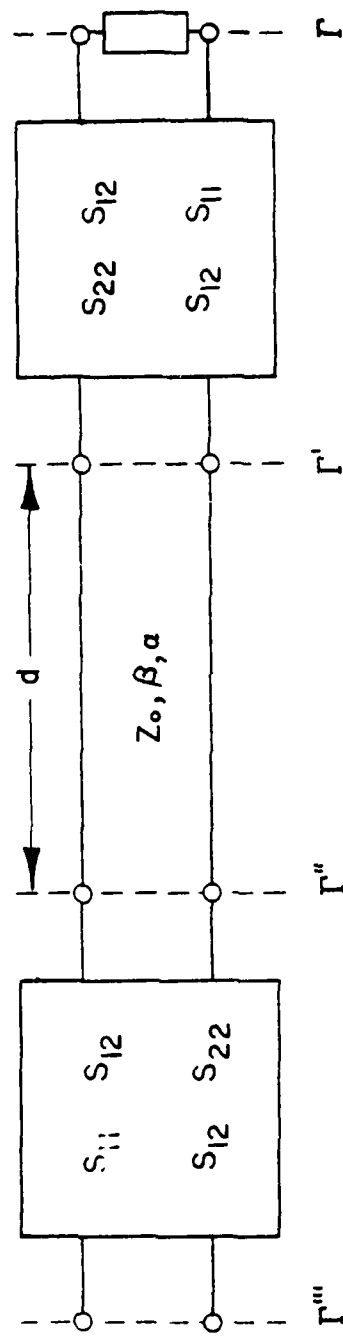


Fig. 4.5. Equivalent circuit for determining scattering parameters of coaxial transition.

Fig. 4.6. In this magnified view, it is easy to see that the points fall on a well-defined circle. The center of the circle is determined from the data by a least square fit.

With  $S_{11}$  determined, the remaining parameters are found by using data taken with the output port shorted. (The short is effected by inserting a hollow brass plug into the connector until it is flush with the Teflon sheath. This is why the junction plane for port 1 was chosen at that position.)  $S_{12}$  and  $S_{22}$  are found by minimizing the residual

$$\Delta \Gamma = S_i \Gamma_i^{\text{measured}} - \Gamma_i^{\text{calculated}}^2 \quad (4.12)$$

where  $\Gamma_i^{\text{measured}}$  is the measured reflection coefficient for  $d = d_i$  and  $\Gamma_i^{\text{calculated}}$  is computed from Equation (4.10) using trial values of  $S_{12}$  and  $S_{22}$ . The scattering parameters were determined for 770 MHz, 800 MHz and 830 MHz and the values are tabulated in Table 4.1. As expected, the discontinuity presented by the transition is rather small and does not vary greatly over the measured frequency range.

With the values of the scattering parameters now known, it is possible to correct the data of Fig. 4.2 and plot the values of return loss and phase that would be measured if there were no discontinuity present. These corrected data are shown in Fig. 4.7. The small improvement in the return loss plot as compared to Fig. 4.2 indicates that the oscillations are not due to the effect of the microstrip launcher. Rather, the departure from linearity must be attributed to system measurement errors. The  $\pm 0.4$  dB excursions in measured data easily fall within the combined error tolerances of the measuring equipment, as stated by the manufacturer. The network analyzer, for example, quotes an accuracy of  $\pm 0.2$  dB, while the 3mm error circle on the polar display CRT translates to at least  $\pm 0.05$  dB.

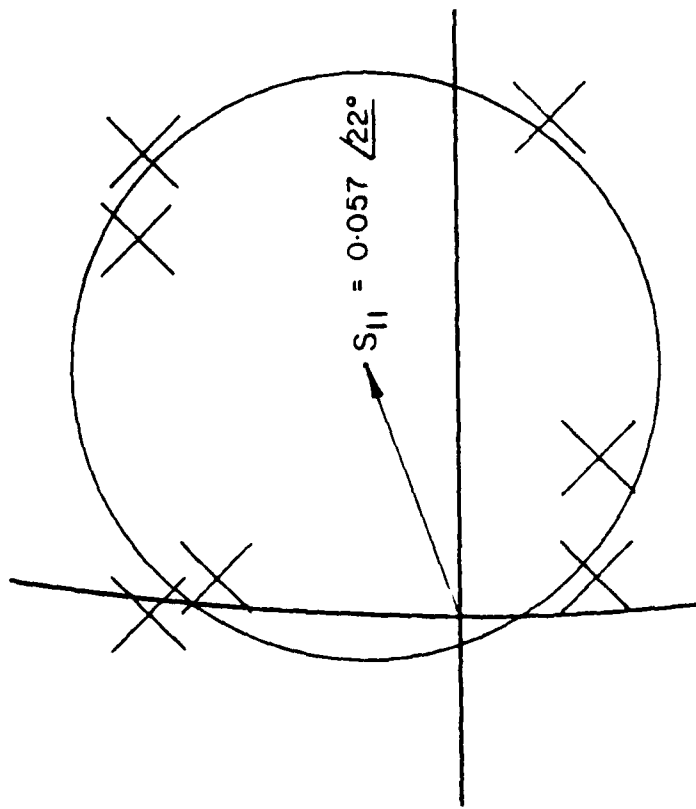


Fig. 4.6. Data used to determine  $S_{11}$  at 800 MHz plotted on central portion of the Smith chart.

Table 4.1: Measured Scattering Parameters

	$S_{11}$	$S_{12}$	$S_{22}$
770 MHz	0.039/ <u>30°</u>	0.997/ <u>-15.2°</u>	0.044/ <u>106°</u>
800 MHz	0.057/ <u>22°</u>	0.998/ <u>-15°</u>	0.046/ <u>117°</u>
830 MHz	0.066/ <u>28°</u>	1.00 / <u>-16°</u>	0.0604/ <u>131°</u>

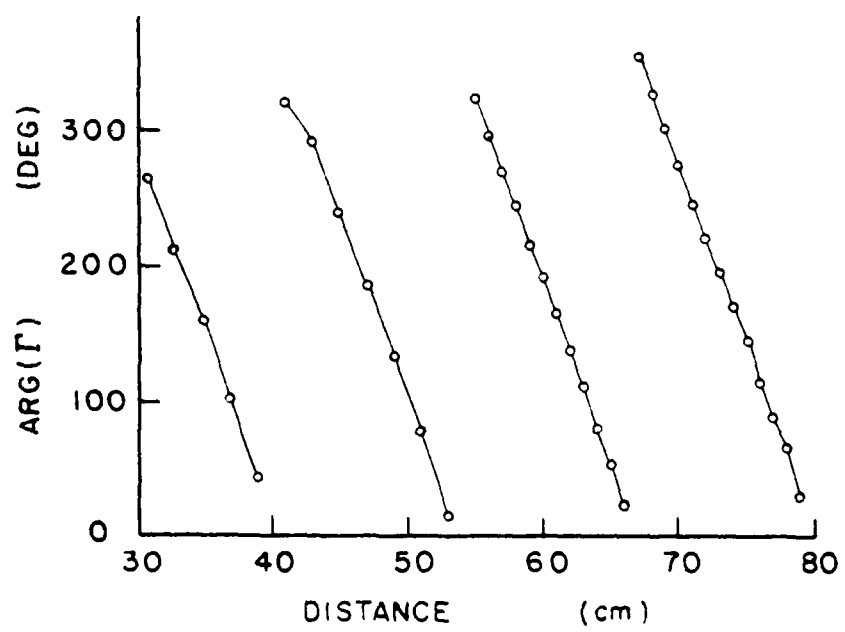
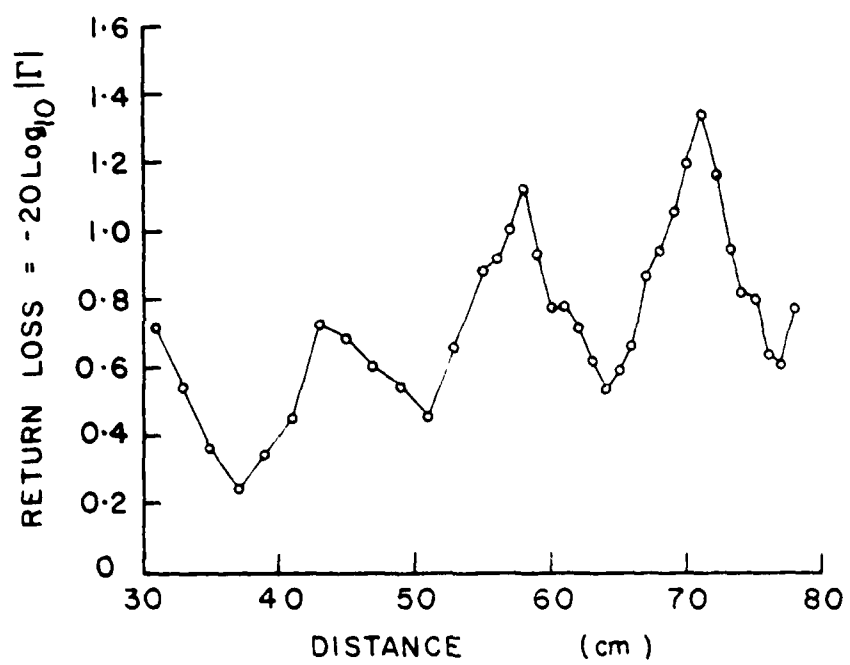


Fig. 4.7. Data of Fig. 4.2 with the effect of the scattering parameters removed.

In this chapter, equations for characterizing microstrip lines have been presented and experimentally verified. The scattering parameters of a microstrip to coaxial line junction have been determined, and it was found that the discontinuity introduces no significant errors in the measurements compared to the measuring system errors. But this investigation has led to an accurate procedure for determining the s-parameters of a small discontinuity.

## V. TWO ELEMENT ARRAY

A basic limitation of microstrip antennas is their inherent narrow bandwidths. In this chapter, the possibility of band-broadening by means of incorporating microstrip elements into an array will be examined.

The basic two element array and its equivalent circuit representation are shown in Fig. 5.1. Using the results of Chapter II, the elements are modeled as parallel RLC resonant circuits with a series inductance connected by lengths of transmission line. The following parameters characterize the circuit:

- $\omega_0^{(i)}$ : the resonant radian frequency of the RLC circuit
- $Q^{(i)}$ : the quality factor of the RLC circuit
- $R^{(i)}$ : the resonant resistance of the RLC circuit
- $L_s^{(i)}$ : the series inductance

where  $i = 1$  for element #1 and  $i = 2$  for element #2.

In terms of these quantities, the input impedance of a single element is

$$z^{(i)} = j\omega L_s^{(i)} + \frac{R^{(i)}}{jQ^{(i)}(\omega/\omega_0^{(i)} - \omega_0^{(i)}/\omega)} \quad . \quad (5.1)$$

The impedance is now transformed through a distance  $d^{(i)}$  on a transmission line with characteristic impedance  $Z_0^{(i)}$ , wave number  $k^{(i)}$  and loss factor  $\alpha^{(i)}$ . After transformation, the impedances of elements 1 and 2 are combined in parallel at the T-junction and the combined impedance is transformed again through the line of length  $d^{(3)}$ , characteristics  $Z_0^{(3)}$ ,  $\beta^{(3)}$ , and  $\alpha^{(3)}$ , to the position of the corporate feed point.

In order to calculate the far field radiation pattern of the array, the relative magnitudes and phases of the currents at the feed point of each

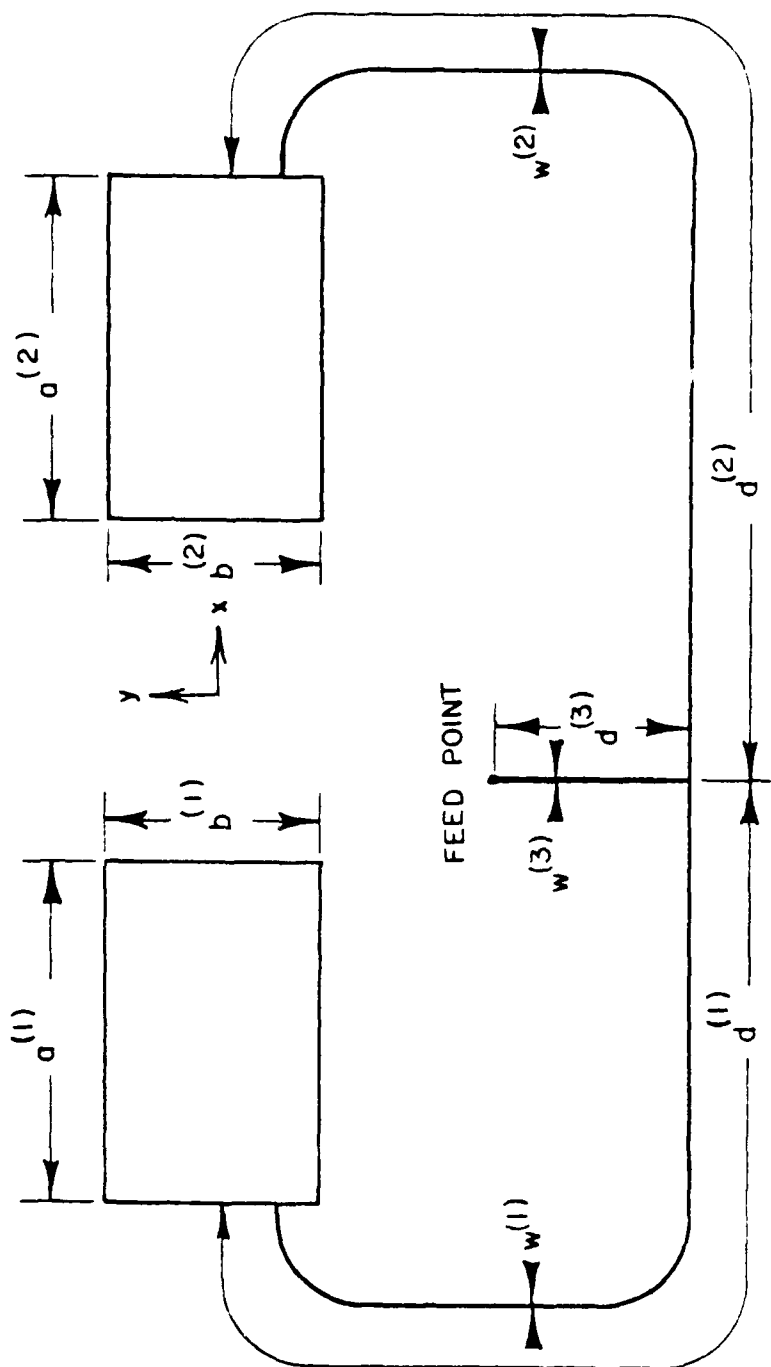


Fig. 5.1. Definitions for two element array.

element must be found. Assuming a total voltage of 1 volt at the T-junction, then  $V_+^{(i)}$ , the positive-going (towards the element) voltage wave on line  $i$ , is found to be

$$V_+^{(i)} = (1 + Z_0^{(i)} / Z^{(i)}) / 2 \quad (5.2)$$

where  $Z^{(i)}$  in Equation (5.2) is the input impedance at the T-junction in line  $=i$ , looking towards element #i. The current at element #i is now easily found to be

$$I^{(i)} = \frac{2V_+^{(i)} \exp(-z^{(i)} + jz^{(i)}) d^{(i)}}{Z^{(i)} + Z_0^{(i)}} \quad (5.3)$$

where  $Z^{(i)}$  in (5.3) is the input impedance of element  $=i$  as given in Equation (5.1).

It is assumed that both elements are of nearly identical dimensions and operating in the (0,1) mode so that the  $z$ -component of the electric field in the x-z plane is the quantity of interest for pattern computation. Then for a single element, and neglecting contributions of non-resonant modes, we find from Equation (2.36) of Chapter II,

$$|E_\phi^{(i)}|_{x-z \text{ plane}} = I^{(i)} \frac{j_{01} \left[ \frac{k_0 \sin \phi}{2} \right] \cos \phi}{k^2 - [k_{01}^{(i)}]^2}, \quad (5.4)$$

where  $a = a^{(1)} \approx a^{(2)}$ . The total pattern is then

$$|E_\phi| = \left| j_{01} \left[ \frac{k_0 \sin \phi}{2} \right] \cos \phi \cdot 1 + \frac{k^2 - [k_{01}^{(2)}]^2}{k^2 - [k_{01}^{(1)}]^2} \cdot \frac{I_1}{I_2} e^{-j(k_0 D_e \sin \phi)} \right|. \quad (5.5)$$

A computer program was written to evaluate the impedance and pattern of the two element array. In order to test the program, an array was constructed with the dimensions shown in Table 5.1. The values of  $\epsilon_0$ , R, Q, and  $L_s$  for

Table 5.1. Array Dimensions

$d^{(1)}$	49.8
$d^{(2)}$	63.5
$d^{(3)}$	5.2
$w^{(1)}$	0.44
$w^{(2)}$	0.44
$w^{(3)}$	0.44
$a^{(1)}$	17.07
$b^{(1)}$	11.39
$a^{(2)}$	16.84
$b^{(2)}$	11.20
$t$	0.15
$\lambda$	0.0036

the elements can be either computed entirely from the theory in Chapters II and III, or measured for several frequencies and then computed using an optimization program that minimized the error between the impedance computed from the simplified Equation (5.1) and the measured input impedance of each element. The agreement between the two has been reported previously [4-6]. Since the objectives of this investigation are first to determine the possible bandbroadening for an array and second to develop a circuit theory for the array design, only the latter method is used. The measured and computed (via Equation (5.1)) values of impedance for element No. 1 fed through a 49.5 cm 50 ohm line are shown in Figure 5.2. Similar agreement is obtained for element No. 2. This result shows that for a narrow band around the resonance, so far as the impedance is concerned, the antenna can adequately be represented by a simple parallel resonant circuit in series with an inductance as given by Equation (5.1).

The computed and measured impedance loci at the feed of the array are shown in Fig. 5.3 and the radiation patterns are plotted for several frequencies in Figs. 5.4 - 5.7. Both impedance loci show the characteristic loop between the resonant frequencies of the two elements. In an optimally designed array, this loop can be used to extend the VSWR-limited bandwidth. However, the pattern is not stable throughout the entire band. Drops of radiation in the broadside direction and tilting of the main beam at some frequency strongly limit the use of this array for broadside radiation application.

The agreement between computed and measured results in Figs. 5.3 - 5.7 is fair. It seems that the program is capable of predicting the general behavior of the array, but cannot track the measured data exactly with frequency. Possible sources of error include dimensional uncertainties, discontinuities introduced by the T-junction and bends in the lines, losses

FREQUENCY INCREASES CLOCKWISE.  
INCREMENT: 5 MHz

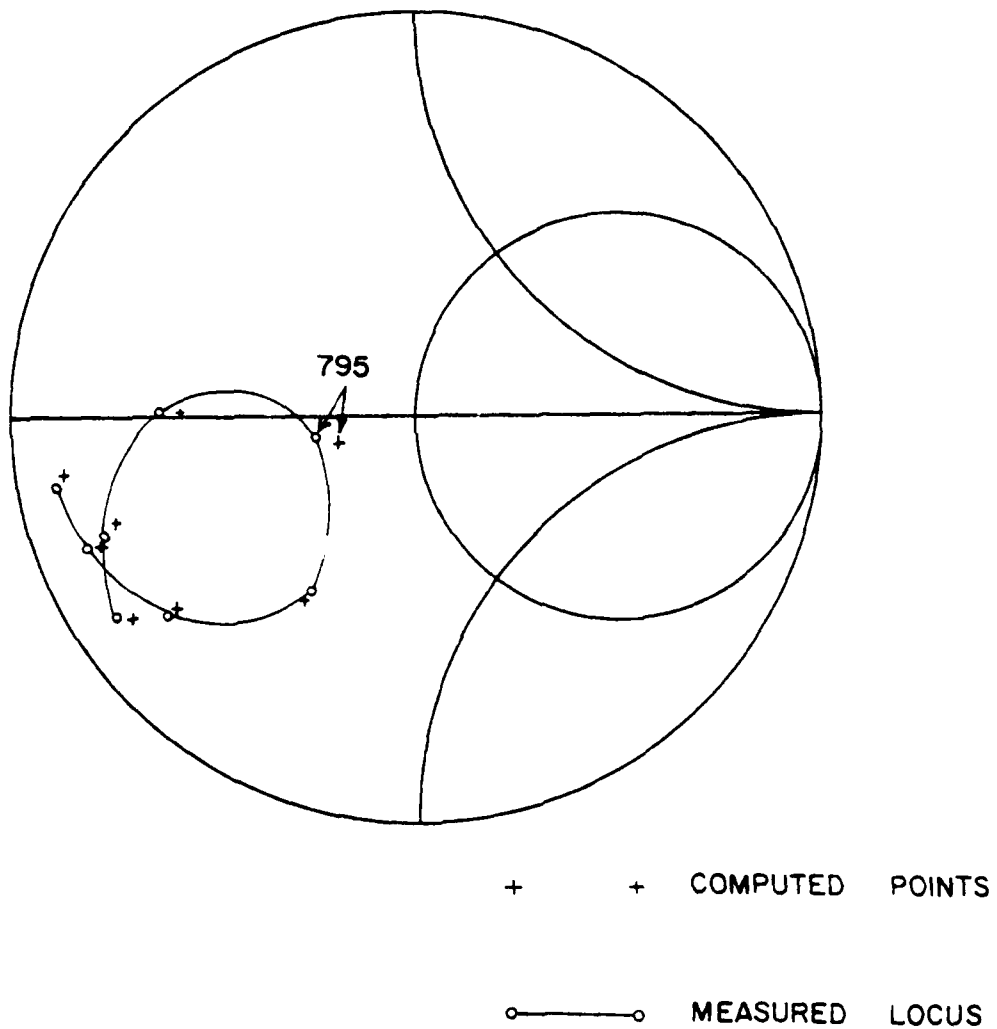
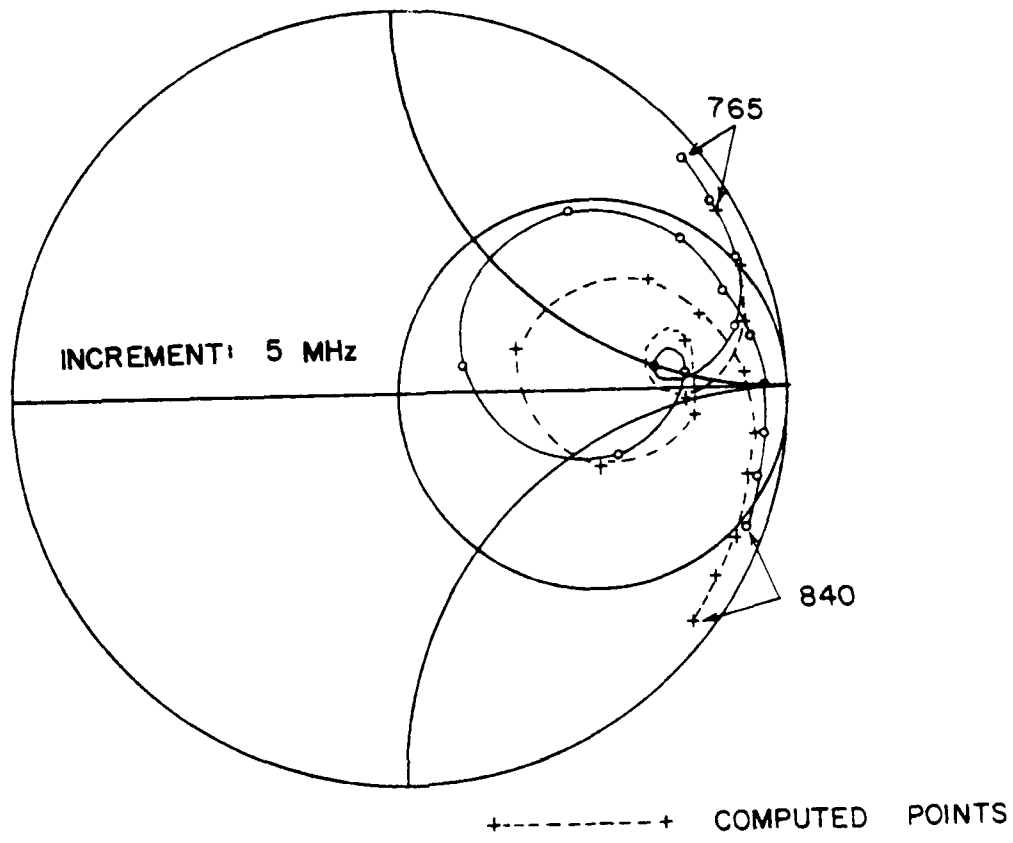


Fig. 5.2. Measured and computed values of  $Z$  for element #1  
with  $d^{(1)} = 49.5$  cm.



○————○ MEASURED LOCUS

$$f_0^{(1)} = 795 \text{ MHz}, \quad f_0^{(2)} = 805 \text{ MHz},$$

$$Q^{(1)} = 90, \quad Q^{(2)} = 91, \quad D_e = 23.6 \text{ cm},$$

$$d^{(1)} = 49.8 \text{ cm}, \quad d^{(2)} = 64.5 \text{ cm}, \quad d^{(3)} = 9.31 \text{ cm},$$

$$w^{(1)} = w^{(2)} = w^{(3)} = 0.44 \text{ cm}, \quad t = 0.15 \text{ cm},$$

$$l = 0.0036 \text{ cm}$$

Fig. 5.3. Measured and computed Z for two element array.

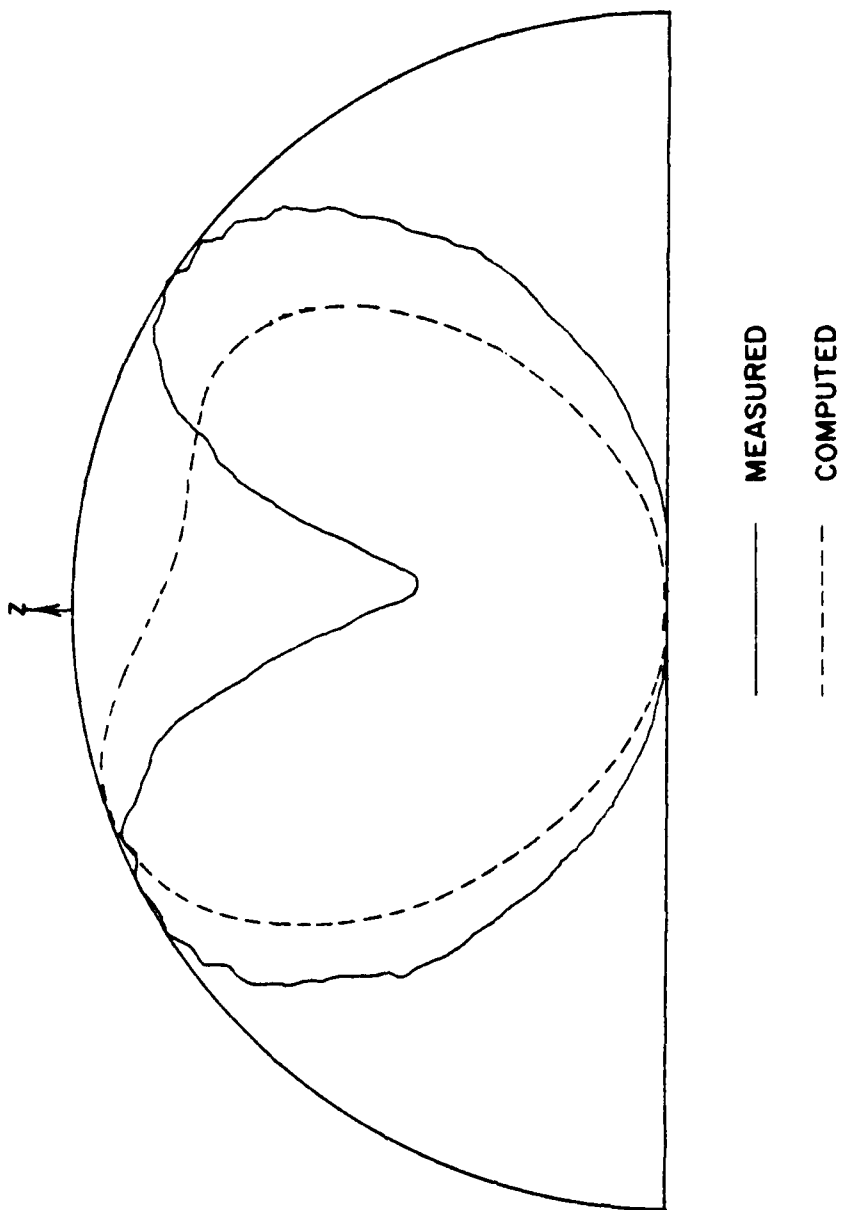


Fig. 5.4. Measured and computed radiation pattern for array at 765 MHz.

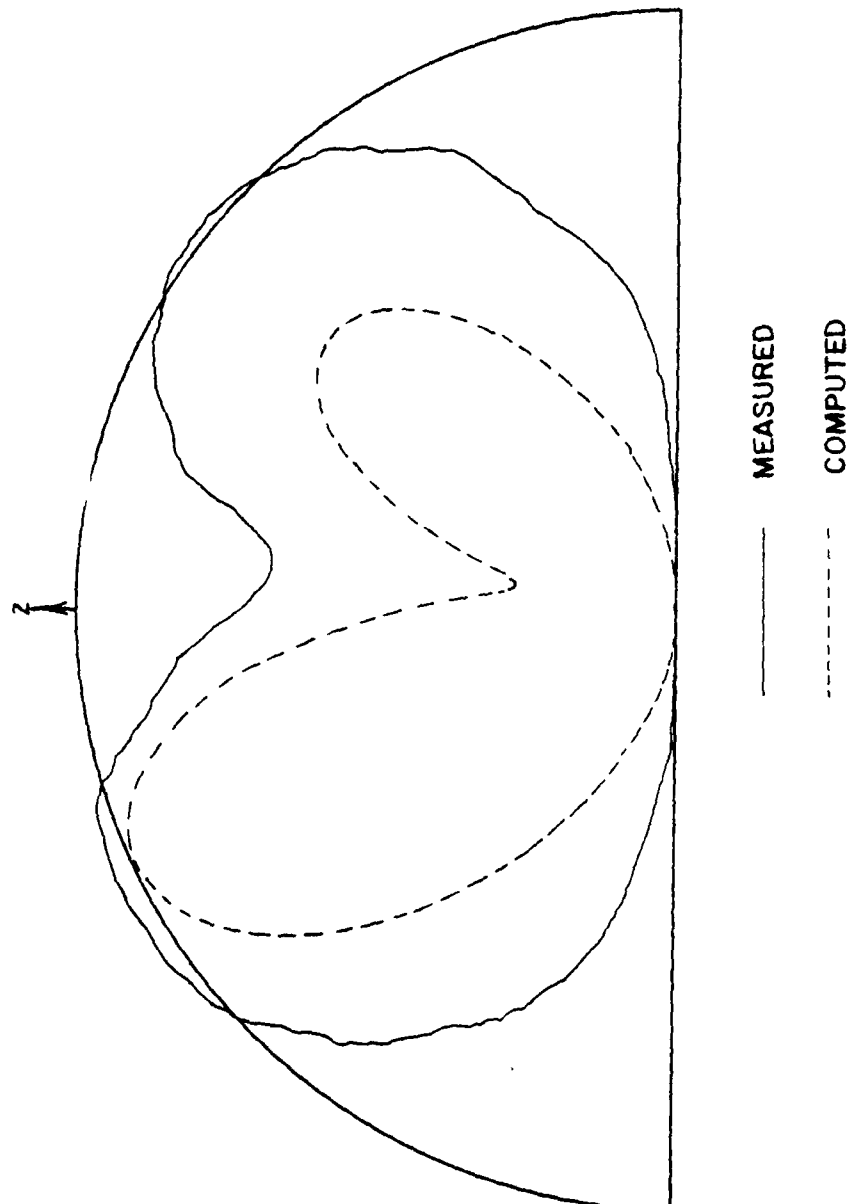


Fig. 5.5. Measured and computed radiation pattern for array at 800 MHz.

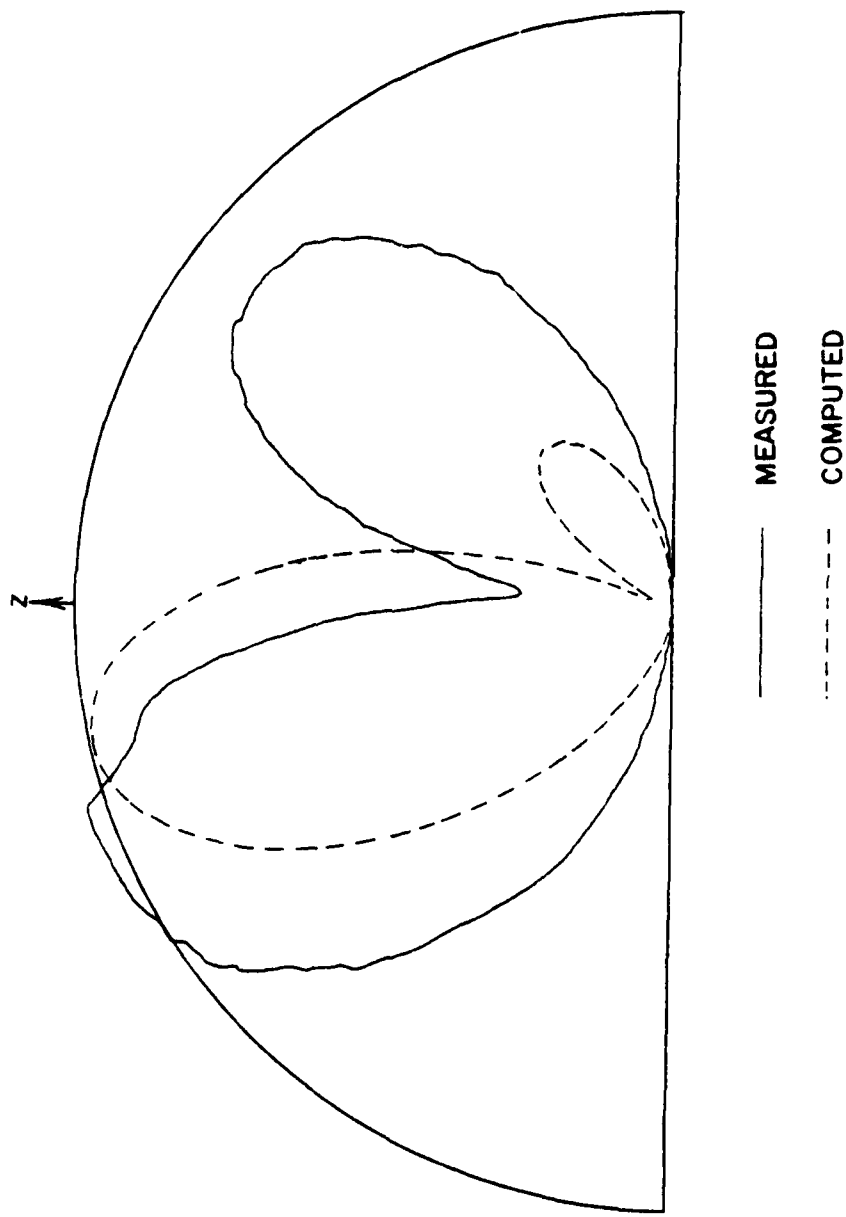


Fig. 5.6. Measured and computed radiation pattern for array at 810 MHz.

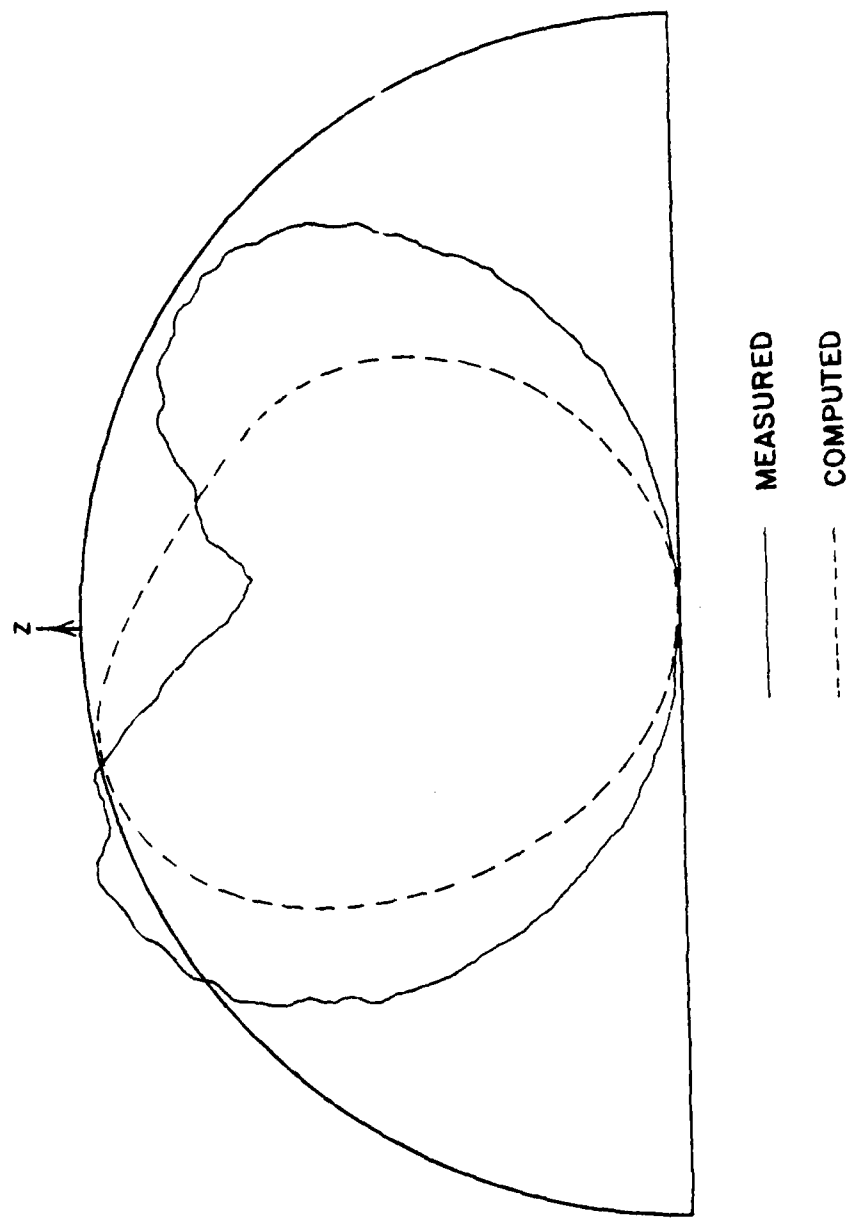


Fig. 5.7. Measured and computed radiation pattern for array at 820 MHz.

due to radiation from the lines, coupling effects between the elements and between the element and the line, and possible inhomogeneity in line and material. Upon perturbing the input data to the program, it was found that both the pattern and the impedance locus change substantially, they are both quite sensitive to small changes in  $d^{(1)}$ ,  $d^{(2)}$ ,  $w^{(1)}$  and  $w^{(2)}$ . Thus, slight inaccuracies in construction or measurement of the array could well have contributed to the discrepancy between measured and calculated results. Nevertheless, the program is a useful design aid, which can be used to test possible array configurations for feasibility.

The use of an array of elements of slightly different dimensions for broadening the bandwidth has been reported recently by Pues, Vandensande, and Van de Capelle [11]. In particular, they considered a two-element array at much higher frequencies, 9 to 10 GHz. It is a simple matter to simulate their array with the present program. A typical pattern so obtained is shown in Figure 5.8 for 9.45 GHz with the designed resonant frequencies 9.00 GHz and 10.0 GHz for the two elements. Note that the beam is skewed from the broadside direction. This effect occurred for all the designs considered. Thus, their claim of stable patterns over the bandwidth is not substantiated by this investigation.

A rather exhaustive search for stable patterns was conducted. The program was modified to determine the best values of  $d^{(1)}$  and  $d^{(2)}$ , leaving their sum unchanged. The T-junction is moved at steps of 0.1 cm, starting with  $d^{(1)} = 2.0$  cm to 20.0 cm. The program was constructed to reject any configuration for which  $E_{\phi}^{(1)}$  and  $E_{\phi}^{(2)}$  differed in phase by more than  $20^\circ$  in the frequency band of interest. It was found that stable patterns could be obtained, but at the expense of larger SWR. For a stable radiation pattern, the loop in the impedance plot would vanish, leaving essentially the bandwidth of a single element.

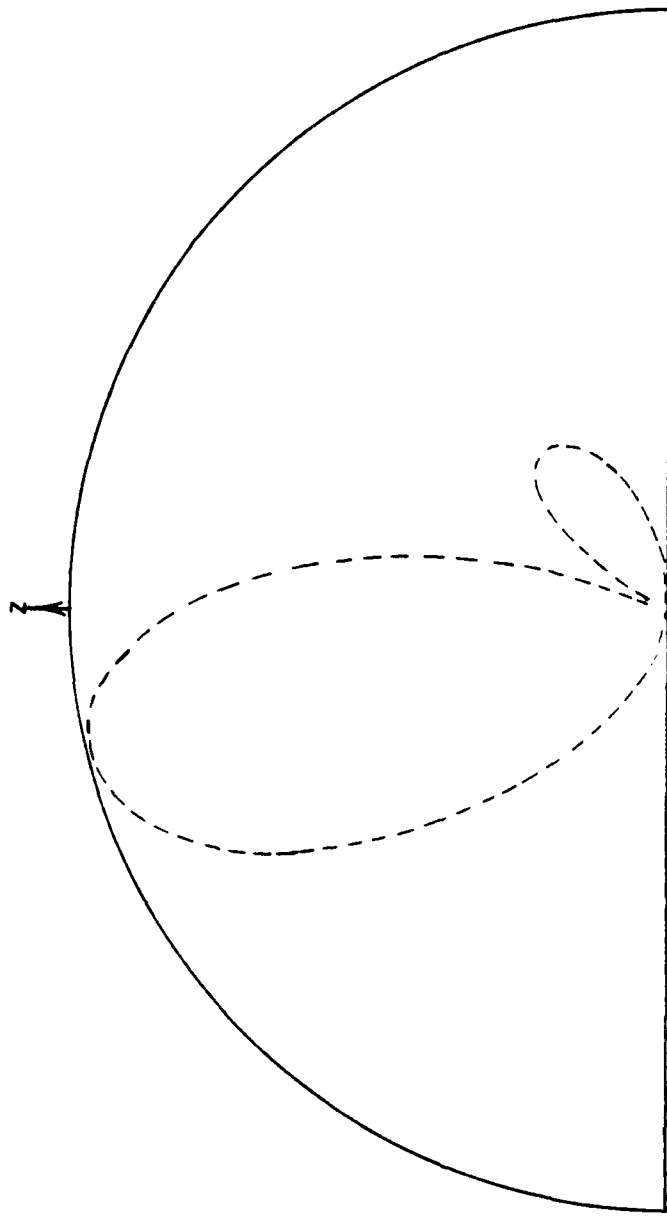


Fig. 5.8. Pattern obtained from design algorithm of Ref. [11] at 9.45 GHz.

In conclusion, it seems that the corporate-fed array of two unidentical elements is not a satisfactory means for broadening the bandwidth of micro-strip antennas.

## VI. SUMMARY

Using the cavity theory of microstrip antennas, a simple explanation for the occurrence of circular polarization has been obtained. Based on this theory, a new type of tunable CP antenna was constructed.

The parameters describing the behavior of microstrip transmission lines were found using closed-form expressions reported in the literature. The scattering parameters of a coaxial to microstrip transition were determined by using a modified classical technique. It was found that for small discontinuities,  $S_{11}$  should be measured with a matched termination, while  $S_{12}$  a shorted (or open) termination; similarly for  $S_{22}$  and  $S_{21}$ . Then they can be computed, using a least square fit for several different measurements. Insofar as this investigation, namely the array feed problem in the microstrip-to-coaxial cable transition, is concerned, the error introduced by this discontinuity is found to be probably smaller than the overall error in our measuring system.

A computer program was written to evaluate the impedance and far-field radiation pattern of a two element microstrip array. Using this program, a design reported in the literature was tested. The algorithm failed to produce a design which had a stable pattern over the frequency band of interest. A search was then conducted for designs yielding stable patterns. It was found that both stable pattern and wide impedance bandwidth seem to be difficult to achieve simultaneously. It may be concluded that corporate-fed arrays of two elements, tuned for slightly different frequencies, do not appear to be a good solution to the bandwidth problem.

## REFERENCES

- [1] J. Q. Howell, "Microstrip Antennas," IEEE G-AP International Symposium Digest, pp. 177-180, December 1972.
- [2] R. E. Munson, "Conformal Microstrip Antennas and Microstrip Phased Arrays," IEEE Trans. Antennas Propagat., vol. AP-22, p. 74, Jan 1974.
- [3] A. G. Derneryd, "Linearly Polarized Microstrip Antennas," IEEE Trans. Antennas Propagat., vol. AP-24, pp. 846-851, Nov. 1976.
- [4] Y. T. Lo, D. Solomon, W. F. Richards, "Theory and Experiment on Microstrip Antennas," IEEE Trans. Antennas Propagat., vol. AP-27, pp. 137-145, March 1979.
- [5] W. F. Richards and Y. T. Lo, "An Improved Theory for Microstrip Antennas and Applications," IEEE AP-S International Symposium Digest, pp. 113-116, June 1979.
- [6] W. F. Richards and Y. T. Lo, "Improved Theory for Microstrip Antennas," Electronics Lett., vol. 15, pp. 42-44, 18 Jan 1979.
- [7] J. L. Kerr, "Microstrip Polarization Techniques," in Proceedings of the 1978 Antenna Applications Symposium, University of Illinois, Urbana, Illinois, Sept. 20-22, 1978.
- [8] R. E. Munson, "Microstrip Antenna Structures and Arrays," U. S. Patent 3,921,177, Nov. 1975.
- [9] H. D. Weinschel, "A Cylindrical Array of Circularly Polarized Microstrip Antennas," in IEEE AP-S International Symposium Digest, pp. 175-180, June 1975.
- [10] P. S. Hall, C. Wood, C. Garrett, "Wide Bandwidth Microstrip Antennas for Circuit Integration," Electron. Lett., vol. 15, pp. 458-459, 19 July 1979.
- [11] H. Pues, J. Vandensande, A. Van de Capelle, "Broadband Microstrip Resonator Antennas," IEEE AP-S International Symposium Digest, pp. 268-271, May 1978.
- [12] R. Courant and D. Hilbert, Methods of Mathematical Physics, vol. I, Interscience, New York, 1953, pp. 275-396.
- [13] P. M. Morse and H. Feshbach, Methods of Theoretical Physics, Part II, McGraw-Hill, New York, 1953, pp. 1360-1432.
- [14] C. C. Johnson, Field and Wave Electrodynamics, McGraw-Hill, New York, 1965, pp. 229-232.
- [15] H. A. Wheeler, "Transmission Line Properties of Parallel Wide Strips by a Conformal Mapping Approximation," IEEE Trans. Microwave Theory Tech., vol. MTT-12, pp. 260-268, May 1964.

- [16] E. Yama snita and R. Mittra, "Variation Method for the Analysis of Microstrip Lines," IEEE Trans. Microwave Theory Tech., vol. MTT-16, pp. 251-256, April 1968.
- [17] A. Farrar and A. T. Adams, "A Potential Theory Method for Covered Microstrip," IEEE Trans. Microwave Theory Tech., vol. MTT-21, pp. 484-496, July 1973.
- [18] E. O. Hammerstad, "Equations for Microstrip Circuit Design," Proc. European Microwave Conference, Hamburg, Germany, pp. 268-272, Sept. 1975.
- [19] R. A. Pucel, D. J. Masse and C. P. Hartwing, "Losses in Microstrip," IEEE Trans. Microwave Theory Tech., vol. MTT-16, pp. 342-350, June 1968.
- [20] M. V. Schneider, "Dielectric Loss in Integrated Microwave Circuits," Bell Syst. Tech. J. 48, No. 7, pp. 2325-2332, Sept. 1969.
- [21] J. E. Storer, L. S. Sheingold and S. Stein, "A Simple Graphical Analysis of a Two-Port Waveguide Junction," Proc. IRE, vol. 41, no. 3, pp. 1004-1013, August 1953.

MISSION  
of  
*Rome Air Development Center*

RADC plans and executes research, development, test and selected acquisition programs in support of Command, Control Communications and Intelligence (C<sup>3</sup>I) activities. Technical and engineering support within areas of technical competence is provided to ESD Program Offices (POs) and other ESD elements. The principal technical mission areas are communications, electromagnetic guidance and control, surveillance of ground and aerospace objects, intelligence data collection and handling, information system technology, ionospheric propagation, solid state sciences, microwave physics and electronic reliability, maintainability and compatibility.

